

High resolution, annual maps of the characteristics of smallholder-dominated croplands at national scales

Lyndon D. Estes*¹, Su Ye^{1,2}, Lei Song¹, Boka Luo^{1,3}, J. Ronald Eastman^{1,3}, Zhenhua Meng¹, Qi Zhang¹, Dennis McRitchie⁴, Stephanie R. Debats⁴, Justus Muhando⁵, Angeline H. Amukoa⁵, Brian W. Kaloo⁵, Jackson Makuru⁵, Ben K. Mbatia⁵, Isaac M. Muasa⁵, Julius Mucha⁵, Adelide M. Mugami⁵, Judith M. Mugami⁵, Francis W. Muinde⁵, Fredrick M. Mwawaza⁵, Jeff Ochieng⁵, Charles J. Oduol⁵, Puren Oduor⁵, Thuo Wanjiku⁵, Joseph G. Wanyoike⁵, Ryan B. Avery⁶, Kelly K. Caylor^{6,7,8}

¹Graduate School of Geography, Clark University, Worcester, MA, USA

²Department of Natural Resources and the Environment, University of Connecticut, Storrs, CT, USA

³Clark Labs, Clark University, Worcester, MA, USA

⁴Independent contributor

⁵SpatialCollective, Nairobi, Kenya

⁶Department of Geography, University of California Santa Barbara, Santa Barbara, CA, USA

⁷Earth Research Institute, University of California Santa Barbara, Santa Barbara, CA, USA

⁸Bren School of Environmental Science and Management, University of California Santa Barbara, Santa Barbara, CA, USA

* *corresponding author*: lestes@clarku.edu

This paper is a non-peer reviewed preprint submitted to EarthArXiv. It will be periodically updated as it is revised, including information on its peer review status.

Abstract

Understanding agricultural change requires reliable, frequently updated maps that describe the characteristics of croplands. Such data are often unavailable for regions dominated by smallholder agricultural systems, which are particularly challenging for remote sensing. To overcome these challenges, we designed a system to minimize several sources of error that arise when mapping smallholder croplands. To overcome errors caused by mismatches between image resolution and cropland scales, as well as persistent cloud cover, the system converts daily, 3.7 m PlanetScope imagery into two seasonal composites within a single agricultural year. To reduce errors that occur when training classifiers, we built a labelling platform that rigorously assesses label accuracy, and creates more accurate consensus labels that train a Random Forests model. The labelling platform and model interact within an active learning process that boosts the accuracy of the resulting cropland probability map, which is used in a segmentation process to delineate individual field boundaries. We applied this system to map Ghana's croplands for the year 2018. We divided Ghana into 16 mapping regions (12,160-23,535 km²), training separate models for each using a total of 6,299 labels, plus 1,600 for validation. Using an independent map reference sample (n=1,207), we found that overall accuracies of the resulting cropland probability and field boundary maps were 88% and 86.7%, respectively, with User's accuracies for the cropland class of 61.2% and 78.9%, and Producer's accuracies of 67.3% and 58.2%. Croplands covered 16.1-23.2% of the mapped area, comprising 1,131,146 total fields with an average size of 3.92 ha. Estimates based on the map reference sample indicate the cropland percentage is 17.1% (15.4-18.9%) or 17.6% (15.6-19.6%), depending on the map used to estimate the standard error. Using the labellers' digitized field boundaries to estimate biases in field boundary statistics, we calculated an adjusted mean field size of 1.73 ha and total field count of 1,662,281. Although the cropland class contained substantial errors, the system was effective in mitigating error and quantifying resulting performance gains. By minimizing training errors, consensus labelling improved the model's F1 scores by up to 25%, while 3 iterations of active learning increased the F1 score by 9.1%, on average, which was 2.3% higher than training models with randomly selected labels. Map accuracy can be improved by replacing Random Forests with a convolutional neural network. These results demonstrate a readily adapted, transferrable framework for developing high resolution, annual, nation-scale maps that provide important details about smallholder-dominated croplands.

1 Introduction

Amidst all the challenges posed by global change, a particular concern is how agricultural systems will adapt to meet humanity's growing food demands, and the impacts that transforming and expanding food systems will have on societies, economies, and the environment (Searchinger et al. 2019). Significant efforts are being made to address the various aspects of this challenge, including work on diagnosing and closing yield gaps (Lobell et al. 2009, e.g. Licker et al. 2010, Mueller et al. 2012), expanding and commercializing production (Morris and Byerlee 2009), and to understand (Rulli and D'Odorico 2014, Kehoe et al. 2017, Davis et al. 2020) and mitigate (Estes et al. 2016b) agriculture's ecological impacts. Answering many of the questions these efforts seek to address depends on reliable data that describes the location and characteristics of cropland (Fritz et al. 2015), and how these are changing over time. Unfortunately, the data that do exist are in many places inaccurate. Existing estimates of how much global cropland there is tend to vary widely, and they often disagree about where cropland is located (e.g. Fritz et al. 2011, 2013). Such errors can propagate in subsequent

44 analyses that rely on cropland data as inputs, resulting in potentially misleading answers (Estes et al.
45 2018). Beyond cropland distributions, few data are available on key cropland characteristics such as
46 field size, an important variable needed to estimate yield and other key food security variables (Carletto
47 et al. 2015), and as an indicator of farm size (Levin 2006, Samberg et al. 2016), a critical component of
48 rural livelihoods given increasing population densities and longstanding debates about the relationship
49 between farm size and productivity (Feder 1985, Carletto et al. 2013, Desiere and Jolliffe 2018).

50 These informational inadequacies are due to the fact that cropland data in much of the world are
51 derived from remotely sensed landcover maps, which can be notoriously high in error, particularly over
52 regions such as Africa (Fritz et al. 2010, Estes et al. 2018), where agricultural changes will be largest
53 and the need for accurate baseline data is thus greatest (Searchinger et al. 2015, Estes et al. 2016b,
54 Bullock et al. 2021). Cropland mapping over Africa is difficult for several reasons. The primary reason
55 relates to the characteristics of the continent’s smallholder-dominated croplands, where half of all fields
56 are smaller than 1 ha (Lesiv et al. 2019). This size is small relative to the 30-250 m resolution of the
57 sensors typically used in many landcover mapping efforts (e.g. Chen et al. 2015, Sulla-Menashe et al.
58 2019), which results in errors due to mixed pixels and aspects of the modifiable area unit problem
59 (Openshaw and Taylor 1979). In the latter case, the pixel’s shape may be poorly matched to that of
60 cropland, and is too coarse to aggregate to approximate that shape at the characteristic scales of crop
61 fields (Dark and Bram 2007, Estes et al. 2018). On top of the matter of scale is 1) high intra-class
62 variability of the cropland class, compounded by the fact that these particular croplands can be heavily
63 intergraded with surrounding vegetation (Debats et al. 2016, Estes et al. 2016a), and 2) the substantial
64 temporal variability within croplands, both within and between seasons. These latter two aspects pose
65 challenges for the classification algorithms that are applied to the imagery.

66 These problems arising from cropland characteristics are increasingly being addressed due to
67 technological advances. Recent advances in satellite technology have increased the coverage of high (<5
68 m) or near-high (10 m) resolution imagery with weekly to near-daily return intervals (Drusch et al.
69 2012, McCabe et al. 2017). This high spatial *and* temporal resolution addresses the sensor-field scale
70 mismatch, and more effectively captures the intra-seasonal dynamics of cropland, which helps classifiers
71 distinguish cropland from surrounding cover types (Debats et al. 2016, Defourny et al. 2019). On top
72 of this, advances in cloud computing (Gorelick et al. 2017), the opening of image archives (Wulder et al.
73 2016), and next generation machine learning approaches (Zhu et al. 2017, Maxwell et al. 2018) are
74 placing large volumes of these moderate to near-high resolution imagery together with the
75 computational and algorithmic resources necessary to classify them at scale. These capabilities are
76 already being used to create a new generation of higher resolution (10-30 m) cropland and landcover
77 maps for Africa and other regions (Xiong et al. 2017, Lesiv et al. 2017, ESA n.d.).

78 Despite these advances, the highest resolution (<5 m) image sources are still not used to map cropland
79 over very large extents, presumably because they are commercial and relatively high cost to acquire, in
80 addition to the greater computational demands. As such, map accuracy can still be a challenge,
81 particular for User’s accuracy, which ranges between 46 and 76% for the cropland class (Xiong et al.
82 2017, e.g. Lesiv et al. 2017).

83 Accuracy may also suffer due to error-inducing factors that are becoming somewhat more pronounced
84 as a consequence of these technology advances, particularly with respect to algorithms. Advances in
85 machine learning are helping to greatly improve classification skill, but these algorithms generally
86 require large, high-quality training datasets (Maxwell et al. 2018, Ma et al. 2019, Elmes et al. 2020).
87 To satisfy this need for more training (and reference) samples, map-makers increasingly rely on visual

88 interpretation of high resolution satellite or aerial imagery to collect training (or validation) samples
89 (Chen et al. 2015, e.g. Xiong et al. 2017, Stehman and Foody 2019). Several web-based platforms have
90 been developed to facilitate such efforts, which provide convenient and highly scalable tools for training
91 data collection (Fritz et al. 2012, Estes et al. 2016a, e.g. Bey et al. 2016). Visually interpreted training
92 labels present two particular problems. The first is that such labels have inevitable interpretation errors
93 that can vary substantially according to the skill of the interpreter (Estes et al. 2016a, Waldner et al.
94 2019). These errors are typically not accounted for in reported accuracy metrics, despite the fact that
95 they can introduce substantial error into the resulting maps and subsequent analyses (Estes et al. 2018,
96 Elmes et al. 2020). The second problem is that visual interpretation depends on high resolution
97 imagery (<5 m), as lower resolutions make it difficult for a human analyst to discern cropland.
98 Typically the only practical source for such imagery are “virtual globe” basemaps provided by Microsoft
99 and Google, which are composed of mosaics of various high resolution satellite and aerial images that
100 typically span 3-5 years of time within a single country (Lesiv et al. 2018). This within-mosaic
101 temporal variation can set up a temporal mismatch between the imagery being interpreted and the
102 imagery being classified, which is usually from a different source (e.g. Landsat, Sentinel; Xiong et al.
103 (2017)). If a land change occurs in the interval between the two image sets (e.g. a new field was created),
104 this can introduce error into the training data that is then passed on to the classifier. This source of
105 error may be elevated in smallholder-dominated systems in the tropics, where swidden practices are
106 common (Van Vliet et al. 2013), or in rapidly developing agricultural frontiers (Zeng et al. 2018).

107 Improving the accuracy of cropland maps over smallholder-dominated systems thus requires an
108 approach that meets three requirements. First, it should be based on high spatial and temporal
109 resolution imagery, to be able to capture the fine grain and temporal variability of smallholders’ fields.
110 Second, an algorithm with suitable skill for classifying these images must be selected, and combined
111 with the computational resources needed to process large imagery volumes. Third, a method for
112 collecting large volumes of high quality training and validation data based on image interpretation is
113 essential. This method should quantify and minimize the errors associated with image interpretation.
114 It should also ensure that labels are collected either from the same imagery that is being classified, or
115 from contemporaneous imagery, in order to reduce errors introduced by land change processes.

116 We describe here a cropland mapping system that follows these requirements, with an emphasis on
117 delineating field boundaries. The first requirement is enabled by the recent availability of CubeSat data
118 that provides 3-4 m resolution imagery over large areas at near daily intervals (McCabe et al. 2017).
119 Although these data, currently collected by Planet’s CubeSat fleet, are of lower spectral depth and
120 quality than Landsat, Sentinel, or Worldview imagery, they enable country to continental scale image
121 mosaics to be created for multiple periods during the crop growing calendars, and capturing the
122 intra-annual variability can be more important for classifying cropland than spectral depth (Debats et
123 al. 2016). This daily revisit capacity is also important for developing seasonal composites in cloudy
124 regions, where satellites with longer return intervals may fail. Lastly, although this imagery being up to
125 ~16 times coarser than much of Bing or Google imagery, it is sufficiently resolved for humans to discern
126 most fields (Fourie 2009, e.g. see Estes et al. 2018). This allows labels to be generated on the same
127 imagery processed by the classifier, thereby addressing one of the two needs related to training data
128 (requirement 3).

129 The second requirement is addressed by a computer vision/machine learning classifier that is effective
130 for classifying smallholder croplands (Debats et al. 2016), re-engineered to run on high performance,
131 cloud-based computing clusters with a simplified feature set, and following recommended practices for
132 controlling for and measuring the errors that occur when training machine learning models for remote

133 sensing applications (Elmes et al. 2020). The classifier is tightly coupled to a front-end platform for
134 collecting label data, which includes rigorous accuracy assessment protocols and a novel approach for
135 merging multiple maps into consensus labels, thereby minimizing image interpretation error (Estes et al.
136 2016a, Elmes et al. 2020). The training and machine learning components are combined within an
137 active learning framework, wherein the machine learning process assesses classification uncertainty in
138 unlabelled areas after a training step, and selects sites from areas of highest uncertainty for additional
139 labelling (Cohn et al. 1994, Tuia et al. 2011). Our framework automates this interactive approach to
140 label selection, which is effective in boosting the performance of classification models while reducing the
141 overall number of training samples required to achieve a given level of performance (Debats et al. 2017,
142 e.g. Hamrouni et al. 2021). Finally, an unsupervised segmentation step is applied to the imagery and
143 merged with the pixel-wise classifications from the machine learning process, resulting in a vectorized
144 field boundary map that provides important information on field geometry.

145 We demonstrate this approach to map cropland in Ghana, a country where smallholder farming
146 predominates, and which has a broad mix of climates and agricultural systems, including large areas
147 where shifting agriculture is practiced (Samberg et al. 2016, Kansanga et al. 2019).

148 **2 Methods**

149 **2.1 System overview**

150 The mapping system design has four primary components focused on 1) image acquisition and
151 compositing, 2) training and validation data collection, 3) image classification, and 4) segmentation.
152 The first component is applied as a once-off step to generate an image catalog covering the mapping
153 geography. The second component provides tools for labelling imagery, and controls an interactive
154 model training and classification (component 3) pipeline that produces a map of cropland probabilities
155 for each image pixel (Figure 1). The final segmentation step (component 4) is then initiated and
156 applied to both the input image catalog and the posterior probability maps, resulting in vectorized field
157 boundaries. Each system component comprises an individual software module designed to be
158 implemented on cloud computing architecture, and available on a GitHub repository (see data and
159 software availability section for details).

160 **2.2 System components**

161 **2.2.1 Image compositing**

162 The image processing components of our system were designed to work with PlanetScope Analytic
163 surface reflectance data (PlanetTeam 2018). PlanetScope provides three visual (red, green, blue) and a
164 near-infrared band at 3-4 m resolution at nominal daily frequency. Although these images are already
165 pre-processed and corrected for atmospheric effects, there are residual errors from inter-sensor
166 differences and the radiometric normalization process (Houborg and McCabe 2018), variation in the
167 orientation of scene footprints, as well as a high frequency of cloud cover over the study region (Wilson
168 and Jetz 2016). To correct for these factors, we developed a procedure for creating temporal composites
169 representing the primary growing and non-growing seasons within a single year.

170 PlanetScope imagery is accessed via the Planet API (PlanetTeam 2018), and an initial order is placed
171 for all imagery falling within the mapping geography and the date ranges for the two compositing
172 periods. The imagery is collected and transferred directly to a cloud storage platform (Amazon Web
173 Services [AWS] S3).

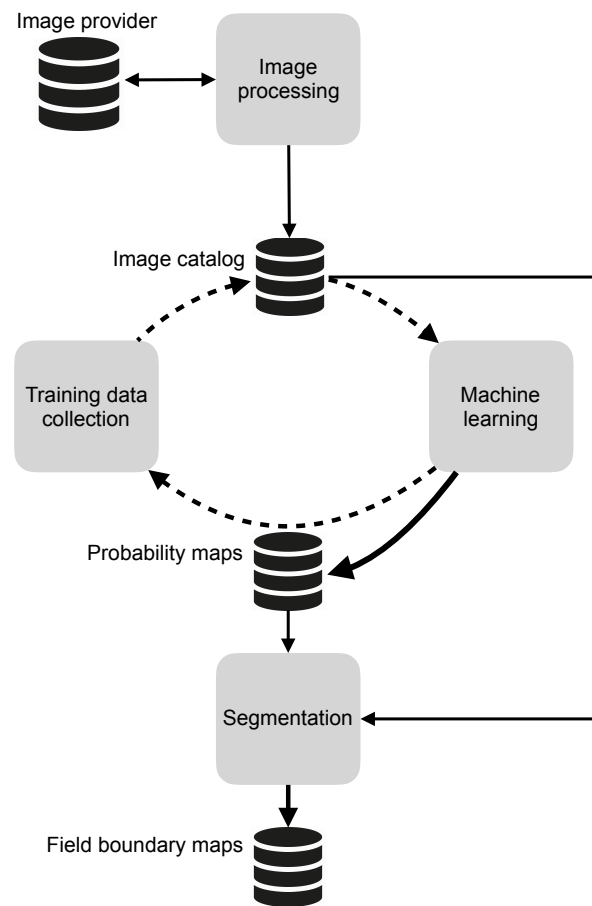


Figure 1: An overview of the primary system components, the data stores that hold the inputs and outputs from each component, and the direction of connections between them. The dashed line indicates iterative interactions, while solid lines indicate one-time or irregular connections.

174 Individual images are then transformed into analysis ready data (ARD) (Dwyer et al. 2018), by
 175 subsetting each downloaded image into 0.05 degree tiles, regardless of cloud cover. Tiles are organized
 176 within a larger 1 degree resolution grid that covers the entire continent, which defines the minimum
 177 mapping area of interest (AOI; Figure 2).

178 The temporal compositing process is applied to the tiled daily images for the time period of interest,
 179 which in this case was one of two multi-month seasons, the primary growing and dry seasons for a
 180 single agricultural year. Imagery from two seasons helps to improve the performance of cropland
 181 classifiers (Debats et al. 2016), while having the seasons in the same year helps to minimize differences
 182 caused by land change. For each pixel in each image in each ARD temporal stack for a given season,
 183 two weights are calculated:

$$W1_t = \frac{1}{blue_t^2} \quad (1)$$

$$W2_t = \begin{cases} \frac{1}{NIR_t^4}, & \text{if } NIR_t < \text{median}\{NIR_{t1}, NIR_{t2}, \dots, NIR_{ti}\}. \\ 1, & \text{otherwise.} \end{cases} \quad (2)$$

184 Where t is a particular date in near-daily time series of PlanetScope images, which begins at date 1 for
 185 the given compositing period and ends on date i , $blue$ is the blue band, and NIR the near infrared band.
 186 Equation 1 assigns lower weights to hazy and clouded pixels as the blue band is sensitive to haze and
 187 cloud pixels (Zhang et al. 2002), while Equation 2 assigns low weights to pixels in cloud shadow
 188 considering the significant darkening effect of the cloud shadows in the Near Infrared band (Zhu and
 189 Woodcock 2012, Qiu et al. 2020)

190 Once these two weights are calculated, the final composited pixel value for each of the four PlanetScope
 191 bands is:

$$\bar{B} = \frac{\sum_{t=1}^T B_t * W1_t * W2_t}{\sum_{t=1}^T W1_t * W2_t} \quad (3)$$

192 Which is a weighted mean for each pixel for each band B for the particular compositing period. The
 193 composited tiles were then added to the S3 store (Figure 1), where they are stored as cloud-optimized
 194 geotiffs, and a “slippy map¹” rendering is created for each composite using Raster Foundry (Azavea
 195 2020). The web-rendered imagery is presented within the training data platform (next section).

196 2.2.2 Labelling platform

197 Training and reference data are collected by a custom labelling platform, which was originally designed
 198 for AWS’s Mechanical Turk job marketplace (Estes et al. 2016a). The basic structure of the system
 199 remains the same, but we converted it into a standalone platform that allows us to enroll and pay
 200 people directly for their labelling, and is designed to control and supervise the machine learning process.
 201 The platform runs on a Linux virtual machine hosted on an AWS EC2 instance and is comprised of a
 202 database (PostGIS/Postgres), a mapping interface (OpenLayers 3), an image server (Raster Foundry),

¹https://wiki.openstreetmap.org/wiki/Slippy_Map

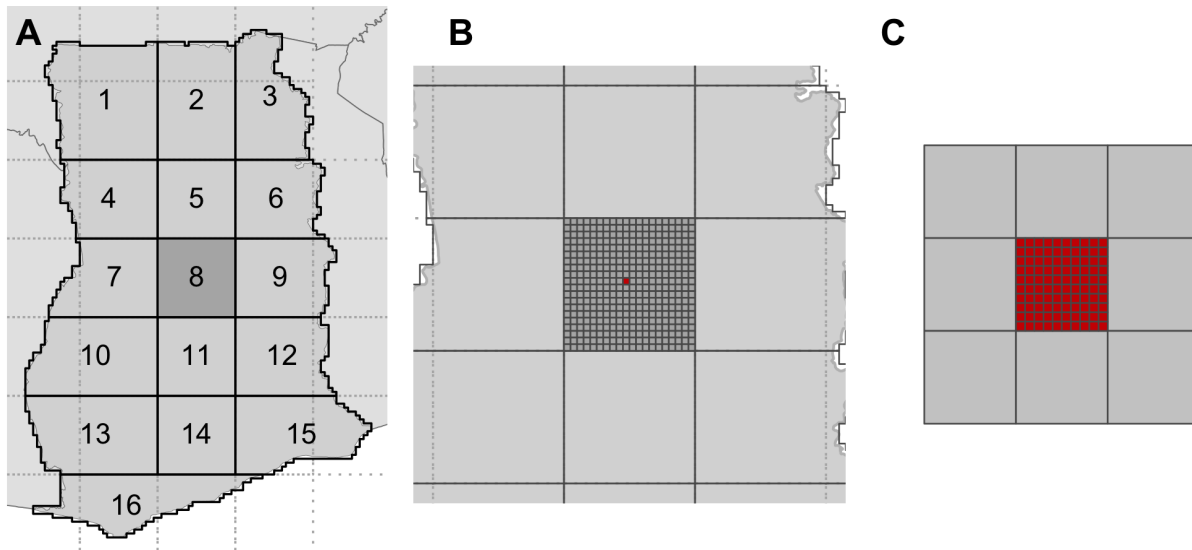


Figure 2: The reference system used in the mapping platform, including A) numbered areas of interest (AOIs) that define the minimum mapping geography (solid black lines; dotted lines indicate boundaries of 1 degree grid), B) the 0.05 degree tile used for compositing imagery, and C) the 0.005 degree resolution reference grid used for collecting training data and distributed computing.

203 and a set of utilities for managing, assessing, and converting digitization work into rasterized labels for
 204 training a machine learning algorithm. Each instance of the platform focuses on a specific AOI (Figure
 205 2A)

206 The following sections provide an overview of the labelling platform’s architecture.

207 2.2.2.1 Mapping workflow

208 **2.2.2.1.1 Selecting training and reference sites** The labelling process begins with the random
 209 selection of a subset (e.g. 500) of cells from a 0.005 degree grid, with the selection itself potentially split
 210 into a training and validation sample, according to predetermined proportions. The grid, which is
 211 nested within the tiling and larger 1 degree grids (Figure 2C) defines the spatial unit for a labelling job.
 212 The selected cells are placed into a queue within the platform’s database, and then converted into a
 213 mapping *task* that has a specified number of *assignments* (boundaries drawn by an individual labeller)
 214 that must be completed before the task is complete.

215 **2.2.2.1.2 Mapping assignments** Labellers registered in the system log in to the mapping
 216 platform (built with Flask) and navigate to the OpenLayers-based field mapping interface (Figure 3),
 217 where they are presented with a white target box representing the randomly selected grid cell, a set of
 218 digitizing tools, and different image backdrops, including true and false color renderings of the growing
 219 season and off-growing season PlanetScope composites, and several virtual globe basemaps. Following a
 220 set of pre-defined digitizing rules (see SI), the labeller uses the polygon drawing tool to digitize the
 221 boundaries of all crop fields intersecting the target grid cell that are visible within the PlanetScope
 222 overlays. To aid with interpretation, the labeller can toggle between the PlanetScope renderings and
 223 the basemaps to help form a judgement about what constitutes a field. The labeller assigns each
 224 polygon a class category (e.g. annual cropland), and upon completing all fields submits the assignment

225 to the database. In cases where the target grid cell does not contain any fields, the labeller simply
 226 submits the assignment to mark it complete. The labeller is then directed to the next available
 227 assignment from a different labelling task.

228 **2.2.2.1.3 Processing completed assignments** All submitted polygons are cleaned to fix
 229 topological irregularities that arose during digitization (see supporting information [SI]) and stored in a
 230 PostGIS table. Each completed assignment represents one of two types of tasks: 1) accuracy
 231 assessment, or 2) model training or validation. For the former type, an accuracy assessment routine is
 232 invoked that executes a series of comparisons between the labeller’s results and a training reference
 233 dataset, resulting in a assignment score:

$$\text{score}_i = \beta_0 I + \beta_1 O + \beta_2 F + \beta_3 E + \beta_4 C \quad (4)$$

234 Where i indicates the particular assignment, and β_{0-4} represent varying weights that sum to 1. I refers
 235 to “inside the box” accuracy, O is the accuracy of those portions of the labeller’s polygons extending
 236 beyond the target grid boundaries, F is fragmentation accuracy, a measure of how many individual
 237 polygons the labeller delineated relative to the reference, E measures how closely each polygon’s
 238 boundary matched its corresponding reference polygon boundary, and C assesses the accuracy of the
 239 labeller’s thematic labels (see SI for individual formulae). Equation 4 is an extension of the approach
 240 described by Estes et al. (2016).

241 Over time, labellers are assessed multiple times across a range of accuracy tasks, which are selected to
 242 represent the variability of the agricultural system being mapped. Each labeller’s score history is
 243 averaged to provide an overall accuracy measure, and this information is used for creating labels, the
 244 second task.

245 If the labeller’s completed assignment was a training/validation task, their maps remain stored in the
 246 database until the task’s outstanding assignments are completed by other labellers. Once complete,
 247 another routine is invoked, which combines the task’s completed assignments into a single consensus
 248 label using a Bayesian merging approach:

$$P(\theta|D) = \sum_{i=1}^n P(W_i|D)P(\theta|D, W_i) \quad (5)$$

249 Where θ represents the true cover type of a pixel (field or not field), D is the label assigned to that
 250 pixel by a labeller, and W_i is an individual labeller. $P(\theta|D)$ is therefore the probability that the actual
 251 cover type is what the labellers who mapped it says it is, while $P(W_i|D)$ is an individual labeller’s
 252 average score over all the accuracy assessment assignments they have completed, and $P(W\theta|D, W_i)$ is
 253 the labeller’s label for that pixel. This approach therefore uses the overall accuracy of each labeller to
 254 weight their labels when combined with those made by other labellers’ for the same pixel (see SI for
 255 further details). As a further measure of confidence in the final consensus label, its average Bayesian
 256 Risk can be calculated (see SI). This measure ranges between 0 and 1, with 0 indicating full agreement
 257 between labellers for all pixels ($n = 40000$) in the label, and 1 indicating complete disagreement.

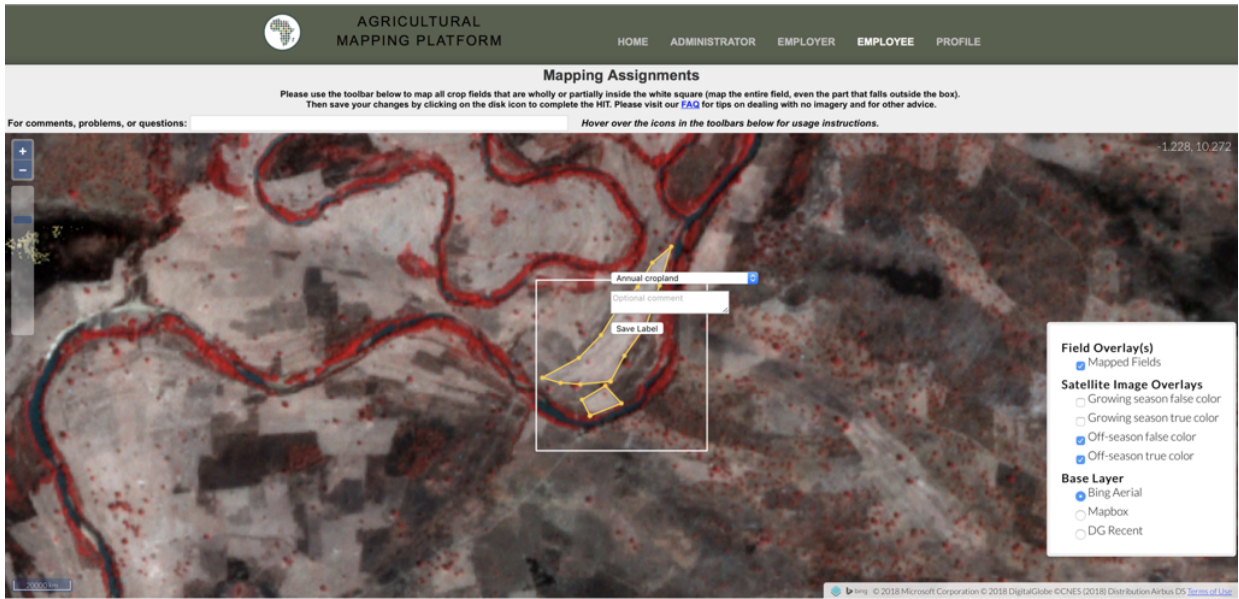


Figure 3: An overview of the labelling platform’s interface

2.2.3 Classification pipeline

Upon completion of a batch of labels, the platform automatically launches an ephemeral Elastic Map Reduce² cluster consisting of tens of instances, depending on the size of the AOI.

2.2.3.1 Feature extraction The first step is the extraction of additional features from each seasonal image composite. Previous work showed that a large number of simple features that summarize the statistical properties of reflectance and vegetation indices in local neighborhoods are highly effective for classifying smallholder croplands (Debats et al. 2016). We followed this logic in this study, but were constrained to use a smaller feature space because the storage and memory requirements for our mapping geographies in this case were several orders of magnitude larger. For this implementation, we thus extract a set of 16 features, which are the mean and standard deviations calculated within an 11X11 and 5X5 moving window, respectively (initial tests revealed these two window sizes to be most effective), resulting in 24 overall features, including the original bands (Table 1).

Table 1. List of image features.

Feature	Window Size	N Features
RGB-NIR	1X1	8
Mean	11X11	8
Standard deviation	5X5	8

Feature extraction and the conversion of image features is handled by a combination of GeoTrellis³, rasterio⁴, and RasterFrames⁵. These collectively extract subsets of imagery from the PlanetScope temporal composites, derive the features, and convert these into Apache Spark DataFrames. Features are extracted on the fly for each cell in the training and validation sets, a functionality enabled by storing the image composites as Cloud-optimized Geotiffs⁶ (COGs).

²<https://docs.aws.amazon.com/emr/latest/APIReference/emr-api.pdf>

³<https://github.com/locationtech/geotrellis>

⁴<https://rasterio.readthedocs.io/en/latest/>

⁵<https://rasterframes.io/>

⁶<https://www.cogeo.org/>

276 **2.2.3.2 Classification** Once the features from the training sites are extracted into `RasterFrames`,
277 these are combined with their corresponding labels and passed to the machine learning classifier, a
278 `SparkMLlib` implementation of Random Forests (Breiman 2001). For this study, the model was trained
279 with a balanced sample and a tree depth of 15 and total tree number of 60, which initial testing showed
280 to provide a reasonable balance between computational time and performance.

281 After fitting, the model is applied to the features of the model validation set, and a set of performance
282 metrics is calculated, including binary accuracy, the F1 score (the geometric mean of precision and
283 recall), and the area under the curve of the Receiver Operating Characteristic (Pontius and Si 2014).

284 **2.2.4 The active learning loop**

285 After fitting and model evaluation a second prediction is undertaken to enable active learning. The
286 feature extraction process is repeated for the rest of the mapping geography that falls outside of the
287 training and validation sample, but applied to a subset of randomly drawn pixels from each cell in order
288 to reduce computational demand. The fitted model is applied to predict the cropland probability for
289 these selected pixels, and an uncertainty criterion (Debats et al. 2017) is calculated for each grid cell:

$$Q_I = \sum_{I(x,y) \in I} (p(x,y) - 0.5)^2 \quad (6)$$

290 Where Q is the uncertainty for grid cell I , calculated from the predicted probability p of the randomly
291 selected subset of pixels (x, y) drawn from it. Pixels with predicted probabilities closer to 0.5 are least
292 certain as to their classification, thus images with the lowest values of Q represent sites posing the most
293 difficulty for the classifier.

294 After scoring with the uncertainty criterion, the top N most uncertain grid cells are selected and sent
295 back to the labelling platform, which are then digitized by the labellers. The resulting consensus labels
296 from the actively selected sample are added to the initial randomly selected sample, and a new cluster
297 is launched. The model is retrained, assesses uncertainty across the remaining unlabelled sites, and
298 selects the next most uncertain sites for labelling. This loop repeats until model performance gains
299 against the validation set show diminishing returns.

300 **2.2.5 Segmentation**

301 After the final iteration, the segmentation algorithm is invoked, which entails several steps. In the first
302 step, the meanshift algorithm (Yizong Cheng 1995) is applied to the original bands of the dry season
303 composite. A Sobel filter is then applied to the green, red, and near-infrared mean-shifted bands and
304 the probability map, and a combined edge image is computed using the sum of these four edge images
305 for the dry season only. A compact watershed algorithm (Neubert and Protzel 2014) is then run on the
306 weighted edge image, with a high level of segmentation specified. In this case, we specified **6400**
307 segments per tile.

308 Third, a region adjacency graph is constructed for each image tile, in which each node represents all
309 pixels within each polygon created in the previous step. The edge between two adjacent regions
310 (polygons) is calculated as the norm of the difference between the means of normalized colors of all
311 bands. Hierarchical merging is then applied, in which the most similar pairs of adjacent nodes are
312 merged until there are no edges remaining below a predetermined threshold of 0.05.

313 In the fourth step, the merged polygons are overlaid with the posterior probabilities resulting from the
314 final active learning loop, and polygons in which the average posterior probability is greater than a
315 predetermined threshold (here 0.5, but could vary locally) are retained as field polygons.

316 In the final step, the retained polygons are refined by removing holes and smoothing their boundaries
317 using the Visvalingam algorithm (Visvalingam and Whyatt 1993). Neighboring polygons that overlap
318 along tile boundaries are then merged.

319 To assess the accuracy of the final segmented boundaries, we used a two-step approach. First, we
320 assessed the overall thematic accuracy of the resulting classification against our map reference data.
321 Second, to assess the quality of the segmentation, we compared the mean area and relative frequencies
322 of the segmented polygons within different size classes against the same metrics derived from the
323 digitized fields of the most accurate worker to create the given map. We selected this relatively simple
324 procedure, as opposed to more complex measures of object accuracy (Ye et al. 2018), because, on the
325 one hand, both the automated segmentation algorithm and labellers are cueing in on the same
326 features—abrupt, physically detectable breaks within the imagery. On the other hand, no matter how
327 well the interpreted/segmented boundaries align with the boundaries of fields in the imagery, it is
328 logistically difficult to evaluate performance against real-world boundaries as the spectral distinction of
329 field boundaries will vary across different crop types and land use arrangements.

330 **2.3 Applying the system to map Ghana**

331 We applied the system to map Ghana’s croplands, excluding areas primarily cultivated with tree crops.
332 Ghana has several distinct agricultural regions, ranging from the primarily grain and vegetable crop
333 producing regions in the northern savannas to tree crop-dominated system in the forested southwest,
334 where cocoa and oil palm are among the dominant crops. For these latter regions, we did not attempt
335 to classify tree crops, and instead mapped clearings that potentially contain field crops or newly felled
336 or recently replanted tree crops. We made this decision because PlanetScope’s resolution is not high
337 enough for labellers to distinguish many tree crops from surrounding forest, and the boundaries of
338 many tree crops (e.g. cocoa) are often not visible.

339 To create the cropland maps, we divided the country into 16 distinct AOIs, which were developed by
340 grouping together each one degree cell fully contained within Ghana with the tiles belonging to any
341 adjacent degree cell that overlapped neighboring countries (Figure 2A). The exception was AOI 16,
342 which consisted of the four degree cells intersecting Ghana’s southern coast. The resulting AOIs ranged
343 from 12,160 to 23,535 km² in extent (average = 15,457 km²), A separate active learning and
344 segmentation process was run for each of these AOIs.

345 To collect the initial randomized samples for model training, we grouped the AOIs into three clusters: a
346 northern cluster comprising the 6 northernmost AOIs (Cluster 1), a central to southeastern cluster
347 (Cluster 2) consisting of the 3 middle (AOIs 7-9) and 2 southeastern AOIs (12 and 15), and a
348 southwestern cluster (Cluster 3) made up of the forest zone AOIs (10, 11, 13, 14, 16). Within each
349 cluster, we randomly selected and labelled 500 grid cells, which provided relatively large initial training
350 samples for these agro-ecologically similar regions, while helping to minimize the overall amount of
351 labelling effort. In addition to these samples, we randomly selected and labelled 100 grid cells within
352 each AOI to provide a validation sample.

353 After collecting the initial training and validation samples, we trained a starter model for each cluster
354 and applied it to each of the block’s AOI. For each iteration, 100 samples were actively selected within

355 each AOI, and added to the training pool.

356 During the collection of training and validation samples, labellers were tasked to only digitize active or
357 recently active crop fields, avoiding tree crops, and fallow or potentially abandoned fields (see SI for the
358 digitizing rules).

359 To evaluate the performance of the system, we performed several analyses described in sections 2.3.1-4.

360 **2.3.1 Image quality**

361 We evaluated the overall quality of the resulting seasonal image composites by assessing a random
362 selection of 50 tiles. We graded both seasonal composites for each tile using a four category quality
363 score, which evaluated the degree of 1) residual cloud and 2) cloud shadow, 3) the number of visible
364 scene boundary artifacts, and 4) the proportion of the image that had its resolution degraded below the
365 typical 3-4 m PlanetScope resolution (e.g. because of between-date image mis-registrations). Each
366 category was qualitatively ranked from 0-3, with 0 being the lowest quality, and 3 the highest (see SI for
367 complete protocol), making the highest possible score 12. We rescaled scores to fall between 0 and 1.

368 **2.3.2 Model gains per iteration**

369 To assess the gain in model performance due to active learning, we measured the change in accuracy,
370 F1, and AUC (see 2.2.3.2) between each iteration and between the first and last iterations for each AOI.

371 To evaluate whether active learning improved model performance relative to a purely random approach
372 to selecting new training sites, we ran additional tests within a subset of AOIs (1, 8, and 15). We first
373 randomly selected and labelled 300-400 sites in each AOI. We then progressively added 100 of the
374 randomly selected samples to the relevant training pool and retrained the model, repeating the process
375 so that the number of iterations and samples matched those from the active learning process. We then
376 compared the difference in accuracy, AUC, and F1 between the randomly trained models and those
377 trained with active learning (Debats et al. 2017).

378 **2.3.3 Accounting for label error**

379 To quantify the potential impact of label error on classification results, we evaluated the performance
380 differences between models trained with three different sets of labels: 1) those from the lowest scoring
381 labeller to map each training site, 2) those from the highest scoring labeller, and 3) the consensus
382 labels. This assessment follows recommended Tier 1 (i.e. best practice) standards to account for
383 training data errors (Elmes et al. 2020).

384 **2.3.4 Accuracy assessment**

385 The model performance assessments described above (2.3.2-3) were not fully independent because they
386 used the same validation sites over multiple iterations (Elmes et al. 2020). To independently assess the
387 accuracy of our final map products, we followed recommended guidelines (Stehman and Foody 2019) to
388 create a separate map reference sample. We used a stratified design, randomly assigning square
389 polygons of ~0.1 ha extent into cropland and non-cropland strata, developed the map of segmented
390 field boundaries. Four classes were used for the map reference sample: cropland; non-cropland; unsure
391 but likely cropland; unsure but likely non-cropland. The latter two classes were used to provide insight
392 into the degree of uncertainty in the map reference sample. For efficiency, two separate supervisors
393 evaluated separate portions of the reference sample, but both jointly assessed a small subset of the

394 sample. We calculated their level of agreement on this subset to provide an additional assessment of
395 uncertainty in the map reference sample (Stehman and Foody 2019). The SI contains further details on
396 the design and collection of the map reference sample.

397 The map reference polygons were then intersected with both the probability images and the segmented
398 field boundaries, and confusion matrixes between the map reference labels and the extracted map
399 classes were constructed to assess the categorical accuracy of each map product. We calculated the
400 overall accuracy for each map, as well as the class-wise User’s and Producer’s accuracy, as well as the
401 95% confidence intervals for each accuracy measure (Olofsson et al. 2013, 2014, Stehman and Foody
402 2019).

403 To assess the accuracy of the segmented field boundaries, we compared the size class distributions of
404 the segmented field boundaries against those of the workers’ digitized polygons at map validation sites.
405 We chose this approach because of existing uncertainties in polygon-based accuracy assessment
406 methods (Ye et al. 2018), and because the map’s ability to represent field sizes was of greatest interest.
407 To undertake this comparison, we selected the field polygons from the most accurate labeller to digitize
408 each of the 100 validation sites in each AOI, and calculated the site-wise average area and number of
409 polygons. We then calculated the same statistics from the segmented boundaries that intersected each
410 validation grid. We compared the distributions and proximity of two measures of central tendency
411 (mean and median) calculated from the two datasets for each AOI, and across all AOIs.

412 **2.4 Assessing the characteristics of Ghanaian cropland**

413 Using the final mapped results, we calculated the estimated area of cropland in Ghana, as well as the
414 average size and total number of fields in the different AOIs. We used the map reference sample to
415 calculate adjusted area estimates and confidence intervals for each map class, and used the differences
416 between labellers’ polygons and segmented boundaries at validation sites to calculate bias-adjusted
417 estimates of mean field sizes and the total number of fields.

418 **3 Results**

419 We developed maps of Ghana’s cultivated croplands within an area of 247,299 km², which included
420 portions of neighboring countries overlapped by images tiles.

421 **3.1 Image catalog and quality**

422 To develop the maps, we first generated an image catalog for the 8,116 tiles covering Ghana. This
423 entailed processing all PlanetScope imagery intersecting these tiles between May-September, 2018 (the
424 growing season) and December, 2018 to February, 2019 (the subsequent dry season). The longer period
425 was necessary for the growing season because of the frequent cloud cover, which substantially limits the
426 number of clear scenes for any tile (Figure S3). For the cloudiest regions (AOIs 10, 11, 13, 14, 16) we
427 started the dry season window in November.

428 An assessment with two observers (see SI for observer details) found that average quality per growing
429 season composite tile was 0.88, with 70 percent having scores ≥ 0.85 , while the average quality of dry
430 season composites was 0.92 (74 percent ≥ 0.85). Composite quality in both seasons was highest in the
431 northern half of the country and lowest in the southwest (Figure 4A), where the substantially greater
432 cloud cover resulted in a much lower density of available PlanetScope imagery for each time period
433 (Figure S3).

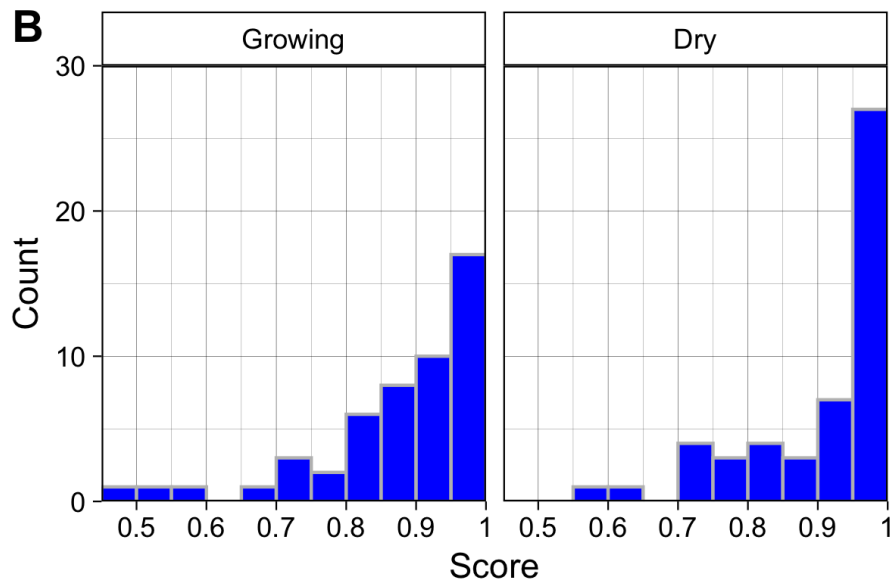
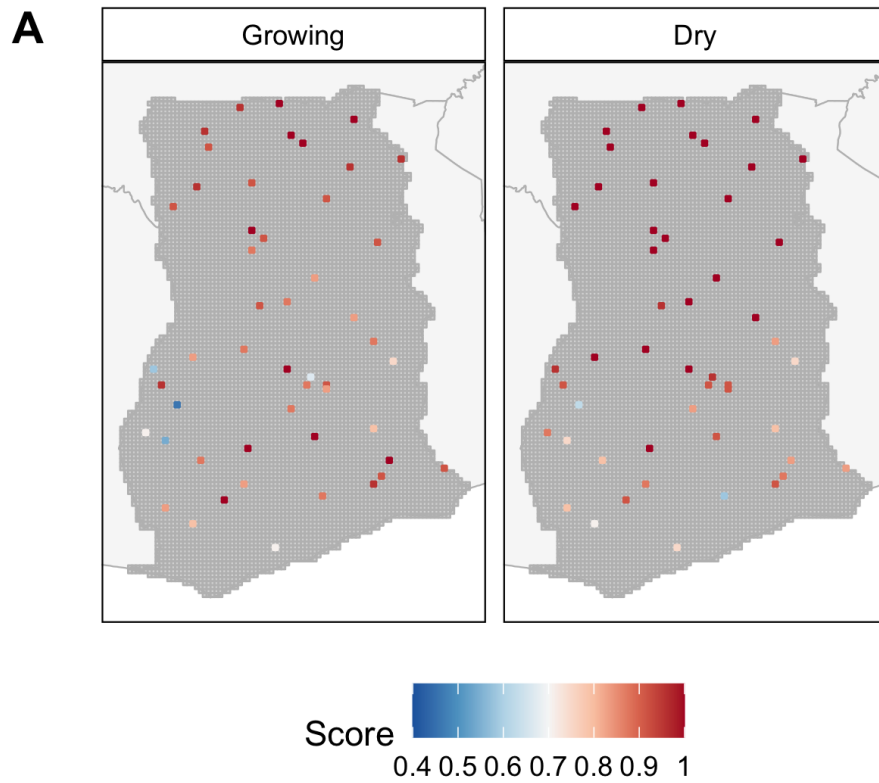


Figure 4: The location and quality scores of 100 randomly selected tiles for the growing (A) and off-growing season (B), and the corresponding distributions of the quality scores for each season, respectively (C and D).

434 **3.2 Active learning**

435 **3.2.1 Training data collection**

436 After training of models with the initial randomly selected label sets, the active learning process was
437 run for 3 iterations for 12 of the 16 AOIs, resulting in 800 labels per AOI. AOIs 10 and 14 stopped after
438 one and two iterations, respectively, as they started with high initial validation accuracies (>83%) and
439 showed little subsequent improvement. The models for these two AOIs were thus trained with 600 - 700
440 samples. AOI 15 was run for 4 iterations (900 samples), while AOI 3 underwent a second active
441 learning cycle because the model produced during the first cycle was inaccurate (see SI). In this second
442 run, 300 initial training sites randomly selected within the AOI were used (Figure S4A), followed by 2
443 subsequent active learning iterations, resulting in a training sample of 500. Labels collected during the
444 active learning iterations showed distinct patterns in several AOIs, which often fell along ecotones, such
445 as the boundaries between agroecozones (see Figure S4A). The total number of unique training and
446 validation sites across the country were 6,299 and 1,600, respectively.

447 The distribution of training and validation sample collection effort was divided across 20 labellers, with
448 a core group of 13 who mapped more than 1,000 sites each. As each training site was mapped by 4
449 separate labellers, 34,014 sets of vector labels were made. Each labeller digitized an average of 2,001
450 (see Figure S5A for more details on labelling effort). Labeller accuracy was scored 9,389 times against
451 98 unique training reference sites (Figure S4A), with each labeller assessed an average of 552 times at a
452 rate of 1 training reference site for every 3.62 training site mapped. The mean of each labeller's average
453 accuracy score was 0.71 (range 0.6 to 0.85; see Figure S5B for detailed score distributions).

454 After each site was mapped by four labellers, consensus labels were generated. The Bayesian Risk (see
455 SI) of each training and validation label was calculated as an additional measure of label quality. The
456 average risk was 0.122 for training labels and 0.127 for validation labels. Risk was highest in the
457 northern AOIs (AOIs 1-6; Figures S6-7), falling between 0.157 for training and 0.173 for validation
458 labels (Figures S6-7), and lowest in the southwestern AOIs (AOIs 10, 11, 13, 14, 16; training risk =
459 0.079; validation risk = 0.065). Label risk in the central-southeastern AOIs (AOIs 7-9, 12, 15) was
460 slightly lower (training = 0.127; validation = 0.136) than in the north. Labeller experience also
461 appeared to reduce risk, which we observed during a relabelling of the 500 initial random site in this
462 cluster (see SI); the mean risk of the updated labels was 0.055, compared to 0.172 for original labels.

463 **3.2.2 Performance gains during active learning**

464 Model performance was calculated for each iteration within each AOI. The average accuracy, AUC, and
465 F1 at iteration 0 were 0.786, 0.809, and 0.464, respectively, increasing to 0.825, 0.818, and 0.507 by
466 iteration 3 (Figure 5). These differences represent respective gains of 4.9, 1.1, and 9.1 percent for the
467 three metrics. The largest gains for each metric occurred on iteration 1, averaging 2.9, 1, and 3.8
468 percent for accuracy, AUC, and F1, while the lowest gains were realized on iteration 3, with accuracy,
469 F1, and AUC respectively increasing by just 1.2%, 0.9%, and 0.3%. The scores achieved on the final
470 iteration varied substantially across AOIs and metrics. Accuracy ranged between 0.725 (AOI 15) and
471 0.948 (AOI 16), while AUC varied from 0.725 (AOI 4) and 0.93 (AOI 11), and F1 from 0.252 (AOI 13)
472 and 0.636 (AOI 8).

473 The comparison of active versus randomized training sample collection (in AOIs 1, 8, and 15) showed
474 that the former approach outperformed the latter. After three iterations, the accuracy, AUC, and F1
475 scores resulting from active learning were respectively 0.8, 0.6, and 2.3 percent higher than the scores

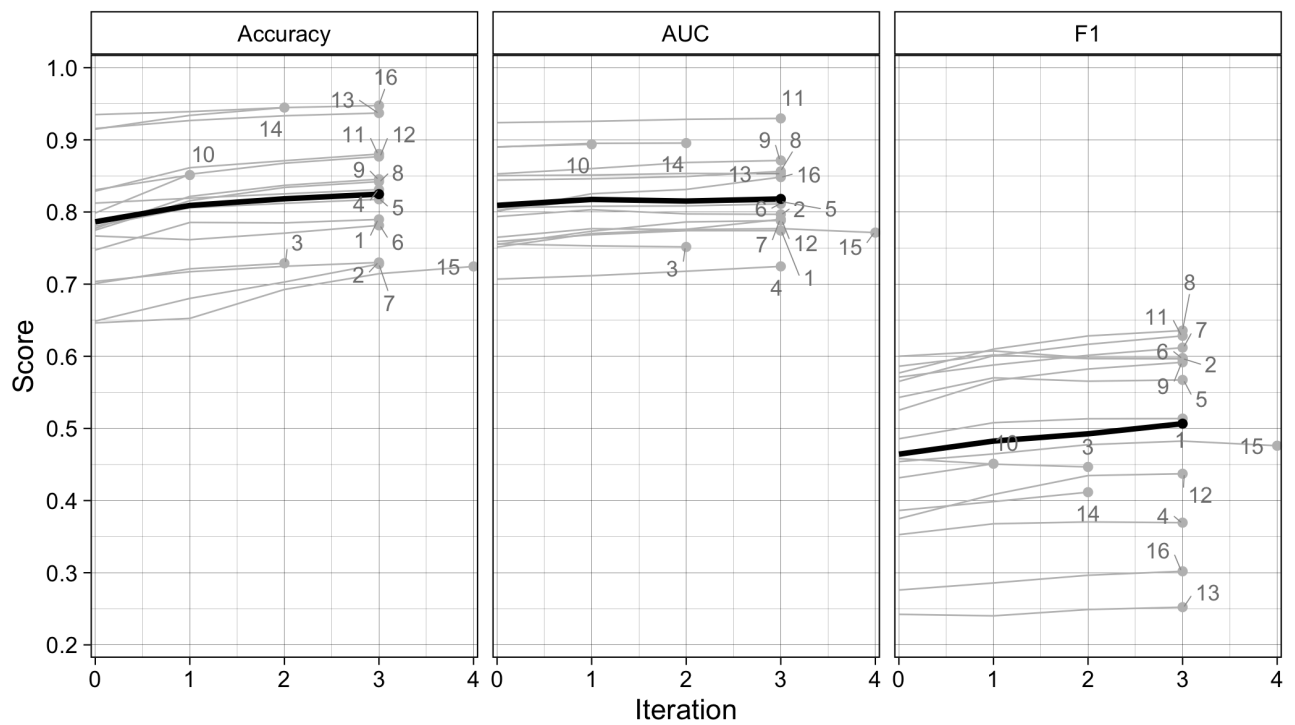


Figure 5: Scores for overall accuracy, area under the curve of the Receiver Operating Characteristic, and the F1 scores for the Random Forests model results after each iteration of the active learning loop for each AOI (gray lines), as well as the mean score per iteration across all AOIs (black lines).

476 from a randomly trained model (Figure S8). However, there was more variability in earlier iterations,
477 with average score differences of -1.7 (accuracy), 0.6 (AUC), and 0.8 percent (F1) after iteration 1, and
478 -0.3 (accuracy), 0.4 (AUC), and 1.8 (F1) percent after iteration 2. The negative results for accuracy
479 was caused by results at AOI 15, where active learning accuracy was 8.37 percent lower than random
480 training after iteration 1 (see Figure 5). In comparison, iteration 1 active learning accuracies were 2.88
481 and 0.45 percent higher than random training for AOIs 1 and 8, respectively. Accuracy under active
482 learning for AOI 15 exceeded randomized training after 4 iterations.

483 3.2.3 The impact of training data error

484 The potential impact of label errors on map quality was assessed in four AOIs (1, 2, 8, and 15). The
485 results of these tests showed that the average accuracy, AUC, and F1 scores for models trained with the
486 consensus labels were respectively 0.772, 0.8, and 0.555 (Figure 6). Performance metrics from
487 consensus-trained models were just 0.5 - 1.2 percent higher than those models trained with the most
488 accurate individuals' labels (accuracy = 0.762; AUC = 0.796; F1 = 0.55), but were 11.6 - 27.4 higher
489 than models trained with the least accurate individual labels (accuracy = 0.606; AUC = 0.716; F1 =
490 0.44).

491 A second measure of the impact of label error is found within the correlations between the mean label
492 risk per AOI and the model performance metrics (Table S3). Accuracy and AUC had strong
493 (Spearman's Rank Correlation = -0.824 to moderate ($r = -0.568$) negative correlations with label risk,
494 while F1 had a weaker but moderate positive association ($r = 0.456$). The positive sign of the latter
495 relationship is counter-intuitive, but is explained by risk's association with precision, one of two inputs
496 to F1, which was moderately positive (0.629), whereas risk had a negligible correlation with recall
497 (0.206), F1's other component. The correlation between risk and the false positive rate (0.688), another
498 important performance metric, shows that labelling uncertainty may increase model commission error.

499 3.3 Map accuracy

500 3.3.1 Categorical accuracy

501 We used a map reference sample of 1207 sites (487 cropland; 720 non-cropland) to evaluate the accuracy
502 of the per-pixel classifications (resulting from thresholding the Random Forests probability), as well as
503 the segmented field boundary maps. We first evaluated the uncertainty in the map reference classes by
504 assessing 1) the overall agreement between map reference labels collected by two separate supervisors at
505 23 sites, and 2) the confidence of the labels assigned by the supervisors (see SI for details). The first
506 measure showed that the two individual supervisors' labels agreed at 87% of common sites, while the
507 second showed that 15.7 of sites were labelled with the two classes that indicated a level of uncertainty.

508 We found that the overall accuracy of the pixel-wise classifications was 88% against this map reference
509 sample (Table 2). Confining the map reference sample to four distinct zones (Figure S10A) shows that
510 overall accuracy ranged from 83.3% in Zone 1 (AOIs 1-3) to 93.6% in Zone 3 (AOIs 10, 11, 13, 15, and
511 16). The Producer's accuracy of the cropland class was 61.7% across Ghana, ranging from 45.6% in
512 Zone 3 to 67.9% in Zone 1, while the User's accuracy for was 67.3% overall, ranging from 59.8% in
513 Zone 4 to 71.2% in Zone 1. Both measures of accuracy were substantially higher for the non-cropland
514 class across all zones, typically exceeding 90%. The lowest accuracies for the non-cropland class was in
515 Zone 1 (Producer's = 89.3%; User's = 87.7%).

516 The overall accuracies obtained from the segmented maps were generally 1-2 percentage points lower

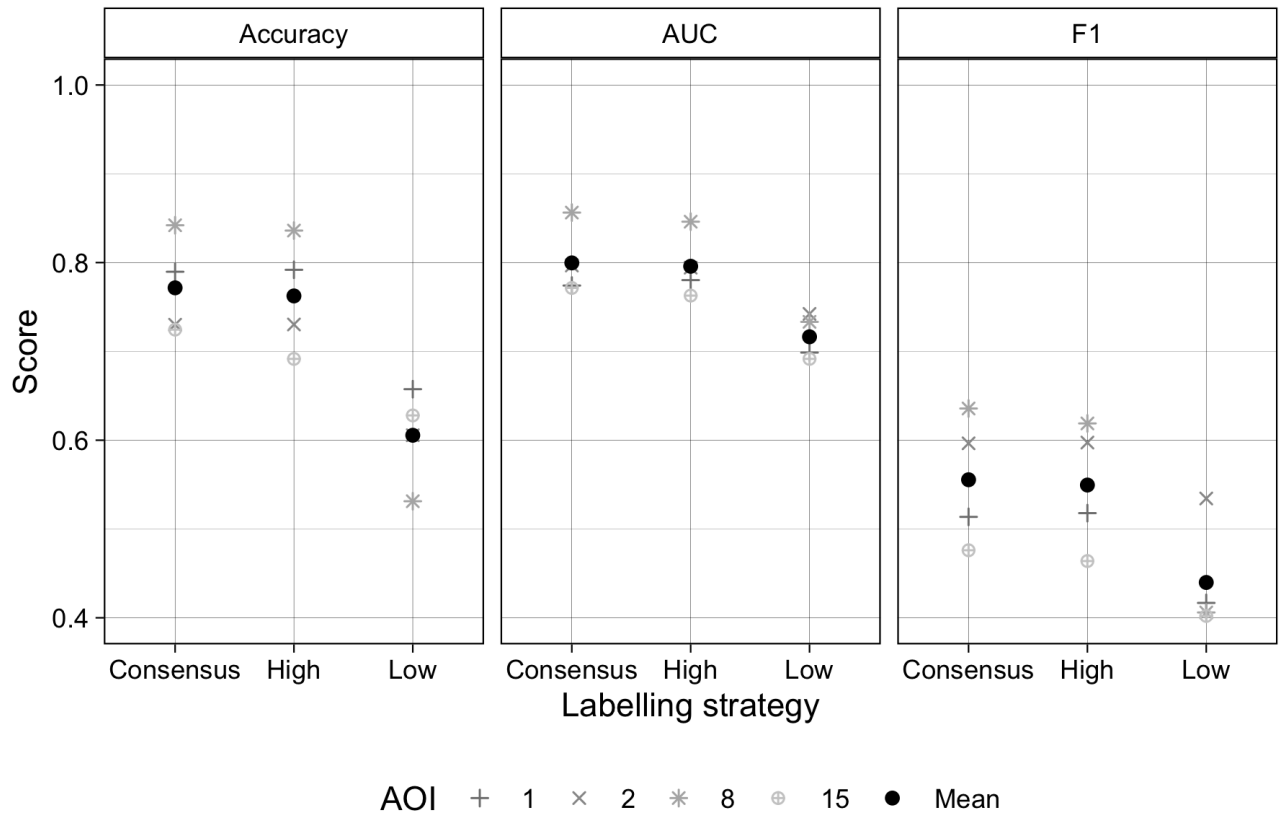


Figure 6: Scores for overall accuracy, area under the curve of the Receiver Operating Characteristic, and the F1 score resulting from models trained with consensus labels, and labels made by the most and least accurate labellers to map each site. Comparisons were made for AOIs 1, 2, 8, and 15, denoted by grey symbols, while the mean scores across these AOIs are shown for each metric.

517 than those of the per-pixel maps, while User’s accuracies tended to be 8-10 percentage points less
518 (Table 2). In contrast, Producer’s accuracies were 15-20 points higher than in the per-pixel map. The
519 segmentation step therefore helped to reduce omission error while substantially increasing commission
520 error.

521 3.3.2 Segmentation accuracy

522 The comparisons of digitized versus segmented field boundaries showed that the mean field size across
523 all validation sites averaged 4.97 ha (Median = 3.75; StDev = 6.04), which was 1.41 times larger than
524 the 2.06 ha (Median = 1.35; StDev = 3.26) mean area of labeller-digitized polygons. This discrepancy
525 was primarily caused by results in four AOIs (2, 3, 7, and 15; Figure S11), where segments averaged
526 between 7.76 and 10.76 ha, compared to 2.18 - 2.77 ha for the corresponding hand-digitized polygons.
527 The number of segmented fields per validation site averaged 3.08 (median = 2.66; StDev = 2.9)
528 compared to 4.4 (median = 3.38; StDev = 4.52) for digitized polygons (Figure S12).

529 3.4 Ghana’s croplands

530 Two separate maps of cropland were produced for each AOI, a per-pixel map derived from the cropland
531 probabilities, and the vectorized map of field boundaries (Figure 7). The former provides the more
532 accurate picture of cropland distributions in Ghana, which are most concentrated in the Southeastern
533 corner (AOI 15), the central-western region (AOI 7, the northeastern and northwestern corners of AOIs
534 10 and 11, and the south of AOI 8), and the northeastern quadrant stretching from AOI 9 through
535 AOIs 5 and 6 and up to AOIs 2 and 3. The northern third of AOI 1 also has noticeable densities of
536 cropland. Several notable areas of low cropland density are also apparent, indicating the presence of
537 large protected areas, such as Mole National Park in the southeastern corner of AOI 1 and Digya
538 National Park in the northwestern corner of AOI 12. In contrast, the relative absence of cropland in
539 AOIs 13, 14, and 16 does not reflect the scarcity of agriculture in these areas, but rather the
540 predominance of tree crops, which we did not map.

541 Both the per-pixel and vectorized maps, when combined with the map reference sample, enable
542 separate estimates of the total extent of croplands in Ghana. The cropland extent estimated from the
543 vectorized map is 42,359 km² (with a margin of error of 4,395 km²), or 17.1 (15.4-18.9%) of the
544 mapped area. The estimate based on the per pixel map is 43,233 km² (margin of error = 4,904 km²),
545 or 17.6 (15.6-19.6%) of area.

546 The vectorized map provides additional information on how the characteristics of croplands can vary
547 geographically, ranging from narrow, strip-like fields in parts of AOI 15 (Figure 7’s lower right inset) to
548 more densely packed, less distinctly shaped fields in AOI 5 (upper right inset in Figure 7). To explore
549 how field characteristics varied geographically, we mapped the average field size and total number of
550 fields within each 0.05 degree tile (Figure S13). These patterns generally correspond to those seen in
551 the cropland density map (Figure 7), with larger sizes and field counts generally occurring in areas of
552 higher field density, although the biases inherent in both measures (Figures S11-12) complicate the
553 interpretation of those variations. However, we can use the estimated biases to develop adjusted
554 estimates of field sizes and counts for each AOI, and for Ghana overall (Table 3). These adjusted
555 estimates show that the typical field size in Ghana is 1.73 ha, ranging from 0.96 in AOI 4 to 2.82 ha in
556 AOI 4, with fields in the forest zone AOIs (10, 11, 13, 14, 16) generally smaller than those in the
557 northern half of the country (Table 3). The total number of fields was estimated to be 1,662,281 overall,
558 or 205 fields per tile on average, ranging from 108/tile in AOI 4 to 399/tile in AOI 6.

Table 2: Map accuracies and adjusted area estimates for the 3 m pixel-wise classifications (based on Random Forests predictions; top 5 rows) and the segmented map (bottom 5 rows). Results are provided for 4 zones (Zone 1 = AOIs 1-3; Zone 2 = AOIs 4-9; Zone 3 = AOIs 10, 11, 13, 14, 16; Zone 4 = AOIs 12, 15) plus the entire country. The error matrix (with reference values in columns) provides the areal percentage for each cell, and the Producer's (P), User's (U), and overall (O) map accuracies and their margins of error (in parenthesis) are provided, as well as the sample-adjusted area estimates (in km²) and margins of error.

		Non-crop	Crop	Total	U		O	n	Area
Per-pixel classification	Zone 1	Non-crop	64.2	9	73.2	87.7 (5.5)	83.3 (4.3)	138	40992 (2468)
		Crop	7.7	19.1	26.8	71.2 (5.9)		226	16025 (2468)
		P	89.3 (5.5)	67.9 (5.9)					
		n	186	178					
	Zone 2	Non-crop	73.9	6.7	80.6	91.7 (4.2)	86.5 (3.6)	169	65123 (2866)
		Crop	6.8	12.6	19.4	64.8 (6.0)		247	15533 (2866)
		P	91.5 (4.2)	65.3 (6.0)					
		n	242	174					
	Zone 3	Non-crop	89.6	4.8	94.4	94.9 (3.2)	93.6 (3.1)	177	70885 (2413)
		Crop	1.6	4	5.6	71.4 (9.0)		98	6860 (2413)
		P	98.2 (3.2)	45.6 (9.0)					
		n	196	79					
	Zone 4	Non-crop	80.7	5.3	85.9	93.8 (5.9)	89.1 (5.3)	65	26473 (1615)
		Crop	5.7	8.4	14.1	59.8 (10.4)		87	4199 (1615)
		P	93.4 (5.9)	61.4 (10.4)					
		n	96	56					
	Ghana	Non-crop	77.2	6.7	83.9	92.0 (2.3)	88.0 (2.0)	549	202856 (4904)
		Crop	5.3	10.8	16.1	67.3 (3.6)		658	43233 (4904)
		P	93.6 (2.3)	61.7 (3.6)					
		n	720	487					
Segmentation	Zone 1	Non-crop	57.6	4.2	61.8	93.2 (5.3)	81.4 (3.9)	88	40890 (2236)
		Crop	14.4	23.8	38.2	62.3 (5.7)		276	15905 (2236)
		P	80.0 (5.3)	84.9 (5.7)					
		n	186	178					
	Zone 2	Non-crop	70.4	3.7	74.1	95.0 (3.9)	85.2 (3.2)	121	65642 (2599)
		Crop	11.2	14.8	25.9	56.9 (5.7)		295	14841 (2599)
		P	86.3 (3.9)	80.1 (5.7)					
		n	242	174					
	Zone 3	Non-crop	86.6	3	89.6	96.6 (2.9)	92.6 (2.8)	148	71695 (2181)
		Crop	4.3	6.1	10.4	58.3 (8.6)		127	7167 (2181)
		P	95.2 (2.9)	66.7 (8.6)					
		n	196	79					
	Zone 4	Non-crop	75.3	3.4	78.7	95.7 (6.0)	86.1 (5.1)	46	26712 (1593)
		Crop	10.4	10.8	21.3	50.9 (9.6)		106	4446 (1593)
		P	87.8 (6.0)	76.0 (9.6)					
		n	96	56					
	Ghana	Non-crop	73.2	3.6	76.8	95.3 (2.1)	86.7 (1.8)	403	204940 (4395)
		Crop	9.7	13.5	23.2	58.2 (3.4)		804	42359 (4395)
		P	88.3 (2.1)	78.9 (3.4)					
		n	720	487					

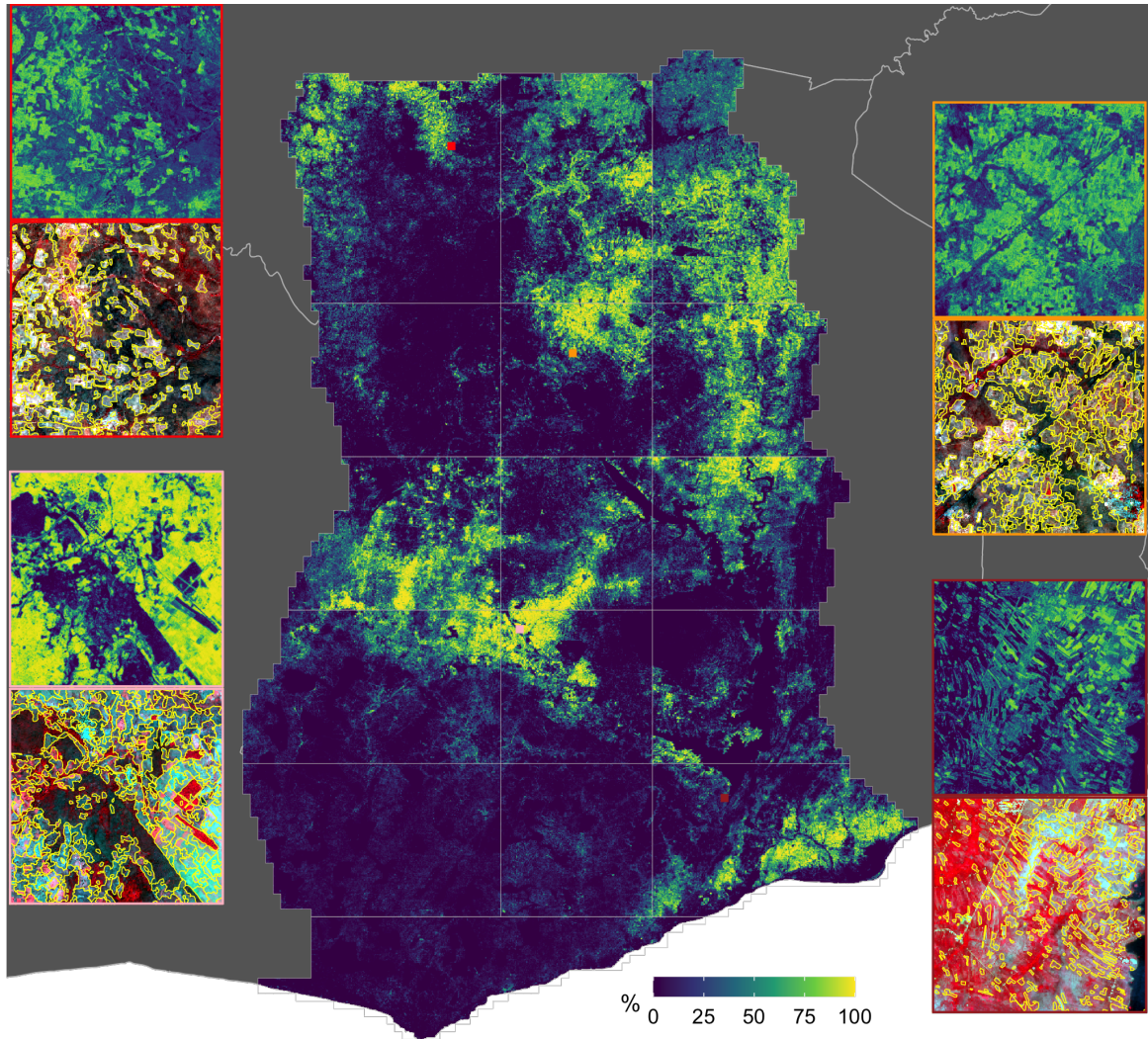


Figure 7: The distribution of croplands in Ghana. The main map shows the percentage of croplands in each 0.005 degree grid cell, derived from the predicted cropland probabilities. The insets on the margins illustrate predicted probabilities (top map in each couplet) at original image resolution (0.000025 degrees) and segmented field boundaries overlaid on the dry season PlanetScope composite, for four separate tiles. Each tile's position is shown on the main map, and is color-coded to the boundary lines around its corresponding inset.

Table 3: The average size and total number of crop fields for each AOI and for Ghana overall. The original and bias-adjusted values for each measure are provided, as well as the total number of 0.05° degree tiles in each AOI.

AOI	N tiles	Size	Size (adj)	N	N / tile	N (adj)	N (adj) / tile
1	777	3.71	1.26	97,822	126	127,580	164
2	597	7.66	1.96	87,666	147	120,651	202
3	501	8.24	2.18	108,819	217	104,422	208
4	465	2.44	2.82	26,276	57	50,163	108
5	400	4.24	2.09	43,290	108	53,756	134
6	429	5.10	2.15	81,363	190	145,347	339
7	471	5.64	1.49	93,282	198	123,005	261
8	400	4.89	1.98	55,500	139	78,868	197
9	479	4.10	1.82	72,081	150	89,840	188
10	630	2.24	1.04	119,019	189	170,907	271
11	400	3.65	1.52	52,510	131	94,709	237
12	471	3.44	1.77	44,667	95	52,947	112
13	627	0.84	0.96	67,996	108	125,368	200
14	400	1.09	2.72	56,006	140	101,767	254
15	548	4.95	1.54	75,752	138	105,681	193
16	521	0.95	1.41	49,097	94	117,268	225
Ghana	8,116	3.92	1.73	1,131,146	139	1,662,281	205

559 4 Discussion

560 These results demonstrate a capability for mapping the characteristics of smallholder-dominated
561 cropping systems at high spatial resolution, annual time steps, and national scales. The resulting maps
562 provide an updated and more granular view of the distribution and extent of croplands in Ghana,
563 complementing existing national to regional land cover maps derived from moderate resolution sensors
564 (Hackman et al. 2017, Xiong et al. 2017, ESA n.d.). This prior work found that cropland covered 19.4
565 (Xiong et al. 2017) to 32% (Hackman et al. 2017) of Ghana in 2015, whereas our 2018 maps have
566 cropland cover of 16.1-23.2% (Table 2), and our map reference sample-based estimates finds 17.1-17.6%
567 cover. Our results thus suggest that Ghana’s cropland is less than previously estimated, but the
568 difference is perhaps attributable to our use of a cropland definition that excluded longer fallows and
569 abandoned fields, which in some regions can account for over half of the total area that could be
570 counted as cropland (Tong et al. 2020).

571 In addition to the more detailed update of cropland extent, our maps also provide new information on
572 the size and number of fields in Ghana (Figures 7, S11-12). Previous work to estimate such agricultural
573 characteristics have often focused on farm, rather than field, size using census data (Von Braun 2004,
574 Samberg et al. 2016, Jayne et al. 2016, Lowder et al. 2016). Efforts to map field boundaries in
575 smallholder-dominated agricultural systems have either used *in situ* data collection (Carletto et al.
576 2013, 2015) or remote sensing studies over relatively small (e.g. Forkuor et al. 2014, Persello et al.
577 2019) or discontinuous (Estes et al. 2016a) areas. The most extensive studies to date used
578 crowdsourced volunteers to classify fields into broad size classes, based on their interpretations of
579 imagery sampled from high resolution virtual globes (Fritz et al. 2015, Lesiv et al. 2019). Those efforts

580 included country-specific results for Ghana ($n = 263$), which can be converted into an average field size
581 estimate of 5.33 ha⁷. This estimate exceeds our Ghana-wide average segment size (3.92 ha; Table 3),
582 but is closer to the mean (4.97 ha) within AOIs 1-9, 12, and 15, which is where most of the
583 crowdsourced sample appears to have been collected. However, our bias-corrected estimates of 1.73
584 (Ghana-wide) and 1.87 (AOIs 1-9, 12, and 15) ha were much smaller.

585 4.1 Map accuracy and key sources of error

586 Although the maps generated by our system provide valuable new information, they nevertheless
587 contain substantial errors. The overall map accuracies (86.7-88%, Table 2) are near the boundary of
588 what might be considered *achievable* map accuracy (Elmes et al. 2020), given the inherent uncertainty
589 in the map reference sample, our best estimate of the “truth,” in which we have roughly 85%
590 confidence. However, accuracies for the cropland class were much lower, falling between 62 (Producer’s)
591 to 67 (User’s) percent country-wide for the per-pixel map (Table 2), meaning the model produced
592 substantial commission and omission errors for this class. The segmented boundary maps had fewer
593 omission errors (Producer’s accuracy = 79%), but higher false positive errors (User’s accuracy =
594 58.2%). These accuracies are near the middle to upper ranges of those reported for the cropland class
595 in other large-area mapping studies (Hackman et al. 2017, Xiong et al. 2017, Lesiv et al. 2017).

596 The patterns of cropland-class accuracies varied by zone. These zones largely align, albeit with some
597 discrepancies, with the country’s agroecozones, thus the accuracy patterns may be partially attributed
598 to some regions being harder to map than others. Producer’s accuracies for both maps were highest in
599 the two northern zones (1 and 2), which are primarily savannas (Figure S10), and lowest in zones 3 and
600 4, which are comprised of forest or coastal savannas. User’s accuracies followed a similar pattern, with
601 the exception of Zone 3, which had the highest User’s accuracy, albeit from a very small sample.
602 Aligning the reference samples more precisely with agroecozone boundaries (Figure S10B) provides
603 further insight into error patterns (Table S4). Coastal savannas in the southeast had the highest
604 Producer’s accuracy but lowest User’s accuracy for the per-pixel map, presumably because this region’s
605 numerous areas of high density cropland, combined with low woody cover in surrounding uncultivated
606 areas, helped to promote commission error. Maps in the two northern savanna agroecozones had the
607 best balance between omission and commission error, and had the highest overall User’s accuracy. The
608 transitional (between forest and savanna) agroecozone had a very low Producer’s accuracy (21%),
609 which likely reflects the fact that it was divided between several AOIs for mapping (Figure S4), within
610 which it typically covered a smaller share of area relative to the other agroecozones. This likely caused
611 insufficient representation of this AEZ in training samples, particularly in AOIs 10 and 11 (Figure S4B).

612 Beyond the errors linked to regional differences, several other important factors contributed to reducing
613 the accuracies in the cropland class. The first of these stems from the overall mapping extent and the
614 high resolution of the data. Given the goal of developing a country-scale map at high resolution, the
615 attendant data volume required us to use a relatively small set of image features and less than the
616 recommended tree number and depth (Maxwell et al. 2018) in our Random Forests implementation, in
617 order to limit computational costs. Previous work found that Random Forests achieves much better
618 performance on small-scale croplands when trained on a much larger number of features (Debats et al.
619 2016). However, applying such a large feature set within the extent of our AOIs was intractable, as the
620 computing time would have been several-fold larger than the ~4-8 hours of runtime on 800 CPUs

⁷Obtained by calculating the weighted mean from the count of the five size classes and the mean of the hectare range provided for the four smallest size classes, and the lower bound of the size range provided the largest size class. Data sourced from Table S3 in Lesiv et al. 2019.

621 required for a single active learning iteration, followed by ~10-14 hours for prediction. This reduced the
622 skill of the model, particularly when it came to differentiating cropland from adjacent bare patches or
623 natural vegetation with sparse herbaceous cover, which were common in many AOIs.

624 The inherent difficulty of the labelling task was another major limiting factor. Our system was designed
625 to minimize the error inherent in labelling, but determining croplands from non-croplands in these
626 agricultural systems can be a difficult task. Labellers have to evaluate multiple image sources and to
627 rely heavily on judgement, which inevitably leads to errors. Interpretation is particularly hard where
628 the background savanna vegetation and croplands have similar reflectance during the dry season, which
629 is a particular problem in AOIs 2 and 3. Smaller field sizes also complicate labelling, as these become
630 increasingly indistinct in the ~4 m PlanetScope composites. The difficulty of labelling is reflected in the
631 magnitude of the Bayesian Risk metrics (Figure S6), and by the average score achieved by each labeller
632 against our training reference dataset (71%; Figure S5B). Although prior work (Rodriguez-Galiano et
633 al. 2012, Mellor et al. 2015) found that Random Forests are robust to label errors, we found that they
634 have substantial impact (Figure 6), which suggest that simply improving label quality may be one of
635 the single most important investments towards improved model accuracy.

636 Image quality was another issue, although primarily in the forested AOIs, where frequent cloud cover
637 reduced the number of available images in all seasons, resulting in composites with more brightness
638 artifacts and blur (Figure 4). This impacted labellers' abilities to discern fields, and doubtless affected
639 model predictions. There is little to be done to mitigate these errors, short of confining imagery to the
640 less cloudy dry season, which may further undermine model performance, given the importance of
641 multi-temporal imagery for cropland classification (Debats et al. 2016, Defourny et al. 2019).

642 Composite quality could be improved by using imagery from the same seasons over multiple years, but
643 this would undermine the goal of developing annual maps, while the dynamism of the croplands would
644 blur field boundaries within the imagery.

645 The final major source of error arose from the segmentation process. The vectorized maps had high
646 commission errors caused by uncertainties in the Random Forests predictions. Model uncertainty led to
647 many pixels over non-crop areas with probabilities straddling the 0.5 classification threshold. Segments
648 that intersected such areas were retained as fields when the average probability of intersecting pixels
649 exceeded 0.5. A more accurate classifier would reduce such errors, or the application of a locally
650 varying classification threshold (e.g. Waldner and Diakogiannis 2020). Over-merging was another
651 source of error in the segmentation algorithm, which in some areas led to overestimated field sizes and
652 unrealistic shapes, particularly in high density croplands (e.g. in AOIs 2 and 8; Figure 7) where the
653 boundaries between adjacent fields are often indistinct in the PlanetScope imagery. Minimizing or
654 preventing merging would help in such cases, although could result in the opposite problem,
655 over-segmentation, and thereby underestimate field size.

656 4.2 Error mitigation features

657 Despite the error sources mentioned above, several features of the system proved effective in mitigating
658 error, leading to a higher overall accuracy than would have otherwise been possible. Label accuracy
659 assessment and consensus labelling appeared to be the most effective error mitigation tools. Label
660 accuracy measures allowed us to quantify the substantial impact of label error on model performance
661 (Figure 6), while consensus labels substantially reduced individual labelling errors, resulting in maps
662 that were more accurate than they would have been had we used individually generated labels.
663 Labeller-specific accuracy measures also helped to improve the quality of the consensus labels, by

664 placing higher weight on labels more likely to be accurate during the merging process, rather than
665 giving equal weight to potentially less accurate labels. The ability to select the most accurate
666 individual labels for a site also allowed us to develop independent estimates of field size to which
667 measures of confidence can be attached (Figure S5B), which we were in turn able to correct estimates
668 of field sizes and numbers (Table 3).

669 The active learning approach helped to improve overall model performance relative to randomized
670 training site selection, in line with findings from two recent efforts (Debats et al. 2017, Hamrouni et al.
671 2021). Although the performance gains relative to randomized model training that we observed were
672 smaller (e.g. Debats et al. (2017) 29% higher model performance after one iteration, and 8% higher on
673 the final iterations), those comparisons were made from lower initial bases, with initial training samples
674 that were less than 1/10 the size, in terms of pixels, of our initial training sample. Our large initial
675 randomly selected sample (500 grid cells) meant that our models were substantially trained before they
676 were exposed to actively selected labels, thereby diluting their impact on performance. Nevertheless,
677 the higher average performance of the active approach across three performance metrics demonstrated
678 its effectiveness. Most notable were the larger improvements seen in the F1 score (Figure S8), a
679 balanced performance metric. Gains in accuracy and AUC were smaller. For accuracy, the reduced
680 advantage was primarily due to active learning being outperformed by randomized training after the
681 first iteration in AOI 15, which proved one of the hardest AOIs to both map and label. Active learning
682 likely resulted in the selection of sites that were harder to label than randomly selected ones, leading to
683 more label error, and thus initially lower model accuracy. However, this deficit was overcome by the 5th
684 iteration. The plateau in AUC gains at 0.5% better than randomized training reflects the findings that
685 active learning reduced both the false and true positive rates, the two inputs to AUC. Although the
686 decline of the false positive rate (30.7% between Iterations 0 and 3) was nearly three times larger than
687 that of the true positive rate (10.9%), AUC should be quite sensitive to the reduction in the latter, as it
688 assesses how the tradeoff between the two rates varies across a full range of possible classification
689 thresholds (Pontius and Si 2014).

690 The detail, temporal precision, and large extent of these maps was enabled by the system’s ability to
691 process PlanetScope data, which is currently the only source of sub-5 meter imagery with daily
692 coverage (McCabe et al. 2017). Daily revisits are important for creating seasonal composites within a
693 single year over cloudy areas. The compositing technique we developed allowed us to develop a
694 complete image catalog for the country representing the two seasons for 2018 agricultural year.
695 Although Sentinel-2 is free, has better radiometric quality, and has sufficiently high resolution (10 m) to
696 accurately classify small-scale agricultural systems (e.g. Defourny et al. 2019, Kerner et al. 2020), its
697 5-day interval may be too infrequent to generate sufficiently cloud-free composites during the growing
698 season over southern Ghana. Sentinel-1 is not affected by the same problem, but labelling fields in
699 more coarsely resolved radar images is challenging.

700 4.3 Lingering questions

701 Several potential issues not addressed in our assessment merit further exploration. One of these is the
702 degree of correspondence between image- and ground-collected labels. However, such comparisons may
703 reveal unresolvable differences between the two perspectives. The highly dynamic nature of many
704 agricultural systems means that relatively narrow differences between the dates of ground- and
705 image-based digitizing campaigns can lead to substantial disagreement between the resulting field
706 boundaries, simply because the fields themselves may have shifted during the interval (Elmes et al.
707 2020). These discrepancies could be further exacerbated by differences in the definition of what

708 constitutes a field, which might vary on the ground depending on who is being asked, or who is doing
709 the collecting. These factors suggest that ground versus image label differences would not necessarily
710 indicate how far image-based labellers were from the “truth.” Nevertheless, a comparison against
711 ground data would help to assess how accurately image-collected labels capture the typical size of fields,
712 and thus merits further investigation for this reason.

713 The temporal discrepancies mentioned above (and discussed in Elmes et al. 2020) are another reason
714 why we chose not to label on basemap imagery (in addition to restrictive usage terms), which is
715 typically several years old (Lesiv et al. 2018). However, we did not assess whether the higher label
716 accuracy one might achieve by digitizing on a <1-2 m resolution basemap would offset model errors
717 caused by temporal mismatches.

718 Another potential issue is the degree to which our assessment of the impact of label error on model
719 performance (Figure 6) was influenced by the validation labels we used, which were generated using the
720 consensus method. This could have confounded the assessment, particularly when comparing models
721 trained with the most accurate individual label and those trained with consensus labels. However, the
722 visual assessment of their resulting probability maps confirm the differences in scores: consensus and
723 most accurate individual labels produce nearly identical maps with relatively high certainty, while low
724 quality labels led to a markedly less certain map (Figure S9).

725 4.4 Next steps

726 The maps presented here represent a version 1 product that is freely available to use, along with its
727 underlying code (see SI for details). These data were developed according to the recommended best
728 practices for training and assessing error in machine learning models (Elmes et al. 2020). In their
729 current form, the maps may be useful for a variety of research applications. For example, analyzing the
730 distributions of values in the probability maps may provide additional insight into the relative extents
731 of active versus fallow croplands (Tong et al. 2020). However, use of these data, particularly for
732 decision-making processes (e.g. cropped area estimates), should be careful to account for the reported
733 errors (Olofsson et al. 2014, Stehman and Foody 2019).

734 To facilitate the next step, generating more accurate version 2 maps, several improvements will be
735 made. The first is to replace Random Forests with a more advanced convolutional neural network
736 (CNN), which can generate and learn from a large number of features representing a variety of spatial
737 scales (Ma et al. 2019). Recent work suggests that a common architecture such as U-Net, when trained
738 to distinguish field edges from interiors and combined with a post-hoc segmentation routine, is effective
739 in delineating field boundaries (Waldner and Diakogiannis 2020). Our system can readily incorporate
740 such a model. The labelling platform already provides the methods needed to develop and assess the
741 quality of labels that include field edges and interior classes, while active learning has proven to be
742 effective for optimizing training datasets for deep learning models (Liu et al. 2017, Cao et al. 2020).
743 Our current framework can be adjusted so that it starts by training a CNN from scratch with a large
744 initial random sample, and then uses a transfer learning approach (Pan and Yang 2010) to update the
745 model with the most informative samples from different AOIs or agroecozones.

746 4.5 Conclusion

747 This work demonstrates a proof of concept for developing high resolution, annual maps of
748 smallholder-dominated croplands at national to regional scales, using a framework that can be readily
749 updated to improve map accuracy as technologies improve. Maps that include information on field

750 boundaries can help improve remote estimation of crop planted area and yield, and provide deeper
751 insights into important socioeconomic aspects of agricultural systems, such as the relationships between
752 agricultural productivity and livelihoods. Such maps will be important for developing an understanding
753 of the rapid agricultural change that is currently unfolding throughout much of the continent.

754 5 Acknowledgements

755 The primary support for this work was provided by Omidyar Network’s Property Rights Initiative, now
756 PLACE. Additional support was provided by NASA (80NSSC18K0158), the National Science
757 Foundation (SES-1801251; SES-1832393), and Princeton University. Computing support was provided
758 by the AWS Cloud Credits for Research program and the Amazon Sustainability Data Initiative.
759 Azavea provided significant contributions in engineering the machine learning pipeline. We thank
760 Meridia for providing information about local cropping systems and the characteristics of fields, and
761 Radiant Earth Foundation for advice and guidance regarding machine learning best practices. We
762 thank Manushi Trivedi, Sitian Xiong, and Tammy Woodard for their contributions to the underlying
763 datasets and methods, and Michelle Gathigi, Omar Shehe, and Primož Kovacic for support and
764 management of the labelling efforts.

765 6 References

- 766 Azavea. 2020. Raster Foundry. <https://github.com/raster-foundry/raster-foundry>.
- 767 Bey, A., A. Sánchez-Paus Díaz, D. Maniatis, G. Marchi, D. Mollicone, S. Ricci, J.-F. Bastin, R. Moore,
768 S. Federici, M. Rezende, C. Patriarca, R. Turia, G. Gamoga, H. Abe, E. Kaidong, and G. Miceli.
769 2016. Collect Earth: Land Use and Land Cover Assessment through Augmented Visual
770 Interpretation. *Remote Sensing* 8:807.
- 771 Breiman, L. 2001. Random Forests. *Machine Learning* 45:5–32.
- 772 Bullock, E. L., S. P. Healey, Z. Yang, P. Oduor, N. Gorelick, S. Omondi, E. Ouko, and W. B. Cohen.
773 2021. Three Decades of Land Cover Change in East Africa. *Land* 10:150.
- 774 Cao, X., J. Yao, Z. Xu, and D. Meng. 2020. Hyperspectral Image Classification With Convolutional
775 Neural Network and Active Learning. *IEEE Transactions on Geoscience and Remote Sensing*
776 58:4604–4616.
- 777 Carletto, C., S. Gourlay, and P. Winters. 2015. From Guesstimates to GPStimates: Land Area
778 Measurement and Implications for Agricultural Analysis. *Journal of African Economies* 24:593–628.
- 779 Carletto, C., S. Savastano, and A. Zezza. 2013. Fact or artifact: The impact of measurement errors on
780 the farm sizeproductivity relationship. *Journal of Development Economics* 103:254–261.
- 781 Chen, J., J. Chen, A. Liao, X. Cao, L. Chen, X. Chen, C. He, G. Han, S. Peng, M. Lu, W. Zhang, X.
782 Tong, and J. Mills. 2015. Global land cover mapping at 30 m resolution: A POK-based operational
783 approach. *ISPRS Journal of Photogrammetry and Remote Sensing* 103:7–27.
- 784 Cohn, D., L. Atlas, and R. Ladner. 1994. Improving generalization with active learning. *Machine*
785 *Learning* 15:201–221.

- 786 Dark, S. J., and D. Bram. 2007. The modifiable areal unit problem (MAUP) in physical geography.
787 *Progress in Physical Geography* 31:471–479.
- 788 Davis, K. F., H. I. Koo, J. Dell’Angelo, P. D’Odorico, L. Estes, L. J. Kehoe, M. Kharratzadeh, T.
789 Kuemmerle, D. Machava, A. de J. R. Pais, N. Ribeiro, M. C. Rulli, and M. Tatlhago. 2020. Tropical
790 forest loss enhanced by large-scale land acquisitions. *Nature Geoscience*:1–7.
- 791 Debats, S. R., L. D. Estes, D. R. Thompson, and K. K. Caylor. 2017. Integrating active learning and
792 crowdsourcing into large-scale supervised landcover mapping algorithms. *PeerJ Preprints*.
- 793 Debats, S. R., D. Luo, L. D. Estes, T. J. Fuchs, and K. K. Caylor. 2016. A generalized computer vision
794 approach to mapping crop fields in heterogeneous agricultural landscapes. *Remote Sensing of*
795 *Environment* 179:210–221.
- 796 Defourny, P., S. Bontemps, N. Bellemans, C. Cara, G. Dedieu, E. Guzzonato, O. Hagolle, J. Inglada, L.
797 Nicola, T. Rabaute, M. Savinaud, C. Udrouiu, S. Valero, A. Bégué, J.-F. Dejoux, A. El Harti, J.
798 Ezzahar, N. Kussul, K. Labbassi, V. Lebourgeois, Z. Miao, T. Newby, A. Nyamugama, N. Salh, A.
799 Shelestov, V. Simonneaux, P. S. Traore, S. S. Traore, and B. Koetz. 2019. Near real-time
800 agriculture monitoring at national scale at parcel resolution: Performance assessment of the
801 Sen2-Agri automated system in various cropping systems around the world. *Remote Sensing of*
802 *Environment* 221:551–568.
- 803 Desiere, S., and D. Jolliffe. 2018. Land productivity and plot size: Is measurement error driving the
804 inverse relationship? *Journal of Development Economics* 130:84–98.
- 805 Drusch, M., U. Del Bello, S. Carlier, O. Colin, V. Fernandez, F. Gascon, B. Hoersch, C. Isola, P.
806 Laberinti, P. Martimort, A. Meygret, F. Spoto, O. Sy, F. Marchese, and P. Bargellini. 2012.
807 Sentinel-2: ESA’s Optical High-Resolution Mission for GMES Operational Services. *Remote*
808 *Sensing of Environment* 120:25–36.
- 809 Dwyer, J. L., D. P. Roy, B. Sauer, C. B. Jenkerson, H. K. Zhang, and L. Lymburner. 2018. Analysis
810 Ready Data: Enabling Analysis of the Landsat Archive. *Remote Sensing* 10:1363.
- 811 Elmes, A., H. Alemohammad, R. Avery, K. Caylor, J. R. Eastman, L. Fishgold, M. A. Friedl, M. Jain,
812 D. Kohli, J. C. Laso Bayas, D. Lunga, J. L. McCarty, R. G. Pontius, A. B. Reinmann, J. Rogan, L.
813 Song, H. Stoyanova, S. Ye, Z.-F. Yi, and L. Estes. 2020. Accounting for training data error in
814 machine learning applied to Earth Observations. *Remote Sensing* 12:1034.
- 815 ESA. (n.d.). ESA CCI LAND COVER S2 prototype Land Cover 20m map of Africa 2016.
816 <http://2016africalandcover20m.esrin.esa.int/>.
- 817 Estes, L., P. Chen, S. Debats, T. Evans, S. Ferreira, T. Kuemmerle, G. Ragazzo, J. Sheffield, A. Wolf,
818 E. Wood, and K. Caylor. 2018. A large-area, spatially continuous assessment of land cover map
819 error and its impact on downstream analyses. *Global Change Biology* 24:322–337.
- 820 Estes, L. D., D. McRitchie, J. Choi, S. Debats, T. Evans, W. Guthe, D. Luo, G. Ragazzo, R. Zempleni,
821 and K. K. Caylor. 2016a. A platform for crowdsourcing the creation of representative, accurate
822 landcover maps. *Environmental Modelling & Software* 80:41–53.

- 823 Estes, L. D., T. Searchinger, M. Spiegel, D. Tian, S. Sickinga, M. Mwale, L. Kehoe, T. Kuemmerle, A.
824 Berven, N. Chaney, J. Sheffield, E. F. Wood, and K. K. Caylor. 2016b. Reconciling agriculture,
825 carbon and biodiversity in a savannah transformation frontier. *Phil. Trans. R. Soc. B* 371:20150316.
- 826 Feder, G. 1985. The relation between farm size and farm productivity: The role of family labor,
827 supervision and credit constraints. *Journal of Development Economics* 18:297–313.
- 828 Forkuor, G., C. Conrad, M. Thiel, T. Ullmann, and E. Zoungrana. 2014. Integration of Optical and
829 Synthetic Aperture Radar Imagery for Improving Crop Mapping in Northwestern Benin, West
830 Africa. *Remote Sensing* 6:6472–6499.
- 831 Fourie, A. 2009. Better Crop Estimates in South Africa. ArcUser Online.
- 832 Fritz, S., I. McCallum, C. Schill, C. Perger, L. See, D. Schepaschenko, M. van der Velde, F. Kraxner,
833 and M. Obersteiner. 2012. Geo-Wiki: An online platform for improving global land cover.
834 *Environmental Modelling & Software* 31:110–123.
- 835 Fritz, S., L. See, I. McCallum, C. Schill, M. Obersteiner, M. van der Velde, H. Boettcher, P. Havlík,
836 and F. Achard. 2011. Highlighting continued uncertainty in global land cover maps for the user
837 community. *Environmental Research Letters* 6:044005.
- 838 Fritz, S., L. See, I. McCallum, L. You, A. Bun, E. Moltchanova, M. Duerauer, F. Albrecht, C. Schill, C.
839 Perger, P. Havlik, A. Mosnier, P. Thornton, U. Wood-Sichra, M. Herrero, I. Becker-Reshef, C.
840 Justice, M. Hansen, P. Gong, S. Abdel Aziz, A. Cipriani, R. Cumani, G. Cecchi, G. Conchedda, S.
841 Ferreira, A. Gomez, M. Haffani, F. Kayitakire, J. Malanding, R. Mueller, T. Newby, A. Nonguierma,
842 A. Olusegun, S. Ortner, D. R. Rajak, J. Rocha, D. Schepaschenko, M. Schepaschenko, A. Terekhov,
843 A. Tiangwa, C. Vancutsem, E. Vintrou, W. Wenbin, M. van der Velde, A. Dunwoody, F. Kraxner,
844 and M. Obersteiner. 2015. Mapping global cropland and field size. *Global Change Biology*
845 21:1980–1992.
- 846 Fritz, S., L. See, and F. Rembold. 2010. Comparison of global and regional land cover maps with
847 statistical information for the agricultural domain in Africa. *International Journal of Remote*
848 *Sensing* 31:2237–2256.
- 849 Fritz, S., L. See, L. You, C. Justice, I. Becker-Reshef, L. Bydekerke, R. Cumani, P. Defourny, K. Erb, J.
850 Foley, S. Gilliams, P. Gong, M. Hansen, T. Hertel, M. Herold, M. Herrero, F. Kayitakire, J. Latham,
851 O. Leo, I. McCallum, M. Obersteiner, N. Ramankutty, J. Rocha, H. Tang, P. Thornton, C.
852 Vancutsem, M. van der Velde, S. Wood, and C. Woodcock. 2013. The need for improved maps of
853 global cropland. *Eos, Transactions American Geophysical Union* 94:31–32.
- 854 Gorelick, N., M. Hancher, M. Dixon, S. Ilyushchenko, D. Thau, and R. Moore. 2017. Google Earth
855 Engine: Planetary-scale geospatial analysis for everyone. *Remote Sensing of Environment* 202:18–27.
- 856 Hackman, K. O., P. Gong, and J. Wang. 2017. New land-cover maps of Ghana for 2015 using Landsat
857 8 and three popular classifiers for biodiversity assessment. *International Journal of Remote Sensing*
858 38:4008–4021.
- 859 Hamrouni, Y., E. Paillassa, V. Chéret, C. Monteil, and D. Sheeren. 2021. From local to global: A
860 transfer learning-based approach for mapping poplar plantations at national scale using Sentinel-2.
861 *ISPRS Journal of Photogrammetry and Remote Sensing* 171:76–100.

- 862 Houborg, R., and M. McCabe. 2018. Daily Retrieval of NDVI and LAI at 3 m Resolution via the
863 Fusion of CubeSat, Landsat, and MODIS Data. *Remote Sensing* 10:890.
- 864 Jayne, T. s., J. Chamberlin, L. Traub, N. Sitko, M. Muyanga, F. K. Yeboah, W. Anseeuw, A. Chapoto,
865 A. Wineman, C. Nkonde, and R. Kachule. 2016. Africa's changing farm size distribution patterns:
866 The rise of medium-scale farms. *Agricultural Economics* 47:197–214.
- 867 Kansanga, M., P. Andersen, D. Kpienbaareh, S. Mason-Renton, K. Atuoye, Y. Sano, R. Antabe, and I.
868 Luginaah. 2019. Traditional agriculture in transition: Examining the impacts of agricultural
869 modernization on smallholder farming in Ghana under the new Green Revolution. *International*
870 *Journal of Sustainable Development & World Ecology* 26:11–24.
- 871 Kehoe, L., A. Romero-Muñoz, L. Estes, H. Kreft, E. Polaina, and T. Kuemmerle. 2017. Nature at risk
872 under future agricultural expansion and intensification. *Nature Ecology and Evolution* 1:1129–1135.
- 873 Kerner, H., G. Tseng, I. Becker-Reshef, C. Nakalembe, B. Barker, B. Munshell, M. Paliyam, and M.
874 Hosseini. 2020. Rapid Response Crop Maps in Data Sparse Regions. arXiv:2006.16866 [cs, eess].
- 875 Lesiv, M., S. Fritz, I. McCallum, N. Tsendbazar, M. Herold, J.-F. Pekel, M. Buchhorn, B. Smets, and
876 R. Van De Kerchove. 2017, November. Evaluation of ESA CCI prototype land cover map at 20m.
877 Monograph, <http://pure.iiasa.ac.at/id/eprint/14979/>.
- 878 Lesiv, M., J. C. Laso Bayas, L. See, M. Duerauer, D. Dahlia, N. Durando, R. Hazarika, P. Kumar
879 Sahariah, M. Vakolyuk, V. Blyshchyk, A. Bilous, A. Perez-Hoyos, S. Gengler, R. Prestele, S. Bilous,
880 I. ul H. Akhtar, K. Singha, S. B. Choudhury, T. Chetri, Ž. Malek, K. Bungnamei, A. Saikia, D.
881 Sahariah, W. Narzary, O. Danylo, T. Sturn, M. Karner, I. McCallum, D. Schepaschenko, E.
882 Moltchanova, D. Fraisl, I. Moorthy, and S. Fritz. 2019. Estimating the global distribution of field
883 size using crowdsourcing. *Global Change Biology* 25:174–186.
- 884 Lesiv, M., L. See, J. Laso Bayas, T. Sturn, D. Schepaschenko, M. Karner, I. Moorthy, I. McCallum, and
885 S. Fritz. 2018. Characterizing the spatial and temporal availability of very high resolution satellite
886 imagery in Google Earth and Microsoft Bing maps as a source of reference data. *Land* 7:118.
- 887 Levin, G. 2006. Farm size and landscape composition in relation to landscape changes in Denmark.
888 *Geografisk Tidsskrift-Danish Journal of Geography* 106:45–59.
- 889 Licker, R., M. Johnston, J. A. Foley, C. Barford, C. J. Kucharik, C. Monfreda, and N. Ramankutty.
890 2010. Mind the gap: How do climate and agricultural management explain the 'yield gap' of
891 croplands around the world? *Global Ecology and Biogeography* 19:769–782.
- 892 Liu, P., H. Zhang, and K. B. Eom. 2017. Active Deep Learning for Classification of Hyperspectral
893 Images. *IEEE Journal of Selected Topics in Applied Earth Observations and Remote Sensing*
894 10:712–724.
- 895 Lobell, D. B., K. G. Cassman, and C. B. Field. 2009. Crop Yield Gaps: Their Importance, Magnitudes,
896 and Causes. *Annual Review of Environment and Resources* 34:179–204.
- 897 Lowder, S. K., J. Scoet, and T. Raney. 2016. The Number, Size, and Distribution of Farms,
898 Smallholder Farms, and Family Farms Worldwide. *World Development* 87:16–29.

- 899 Ma, L., Y. Liu, X. Zhang, Y. Ye, G. Yin, and B. A. Johnson. 2019. Deep learning in remote sensing
900 applications: A meta-analysis and review. *ISPRS Journal of Photogrammetry and Remote Sensing*
901 152:166–177.
- 902 Maxwell, A. E., T. A. Warner, and F. Fang. 2018. Implementation of machine-learning classification in
903 remote sensing: An applied review. *International Journal of Remote Sensing* 39:2784–2817.
- 904 McCabe, M. F., M. Rodell, D. E. Alsdorf, D. G. Miralles, R. Uijlenhoet, W. Wagner, A. Lucieer, R.
905 Houborg, N. E. C. Verhoest, T. E. Franz, J. Shi, H. Gao, and E. F. Wood. 2017. The future of
906 Earth observation in hydrology. *Hydrology and Earth System Sciences* 21:3879–3914.
- 907 Mellor, A., S. Boukir, A. Haywood, and S. Jones. 2015. Exploring issues of training data imbalance
908 and mislabelling on random forest performance for large area land cover classification using the
909 ensemble margin. *ISPRS Journal of Photogrammetry and Remote Sensing* 105:155–168.
- 910 Morris, M., and D. Byerlee. 2009. *Awakening Africa’s Sleeping Giant*. World Bank and FAO,
911 Washington, DC.
- 912 Mueller, N. D., J. S. Gerber, M. Johnston, D. K. Ray, N. Ramankutty, and J. A. Foley. 2012. Closing
913 yield gaps through nutrient and water management. *Nature* 490:254–257.
- 914 Neubert, P., and P. Protzel. 2014. Compact Watershed and Preemptive SLIC: On Improving Trade-offs
915 of Superpixel Segmentation Algorithms. Pages 996–1001 2014 22nd International Conference on
916 Pattern Recognition. IEEE, Stockholm, Sweden.
- 917 Olofsson, P., G. M. Foody, M. Herold, S. V. Stehman, C. E. Woodcock, and M. A. Wulder. 2014. Good
918 practices for estimating area and assessing accuracy of land change. *Remote Sensing of*
919 *Environment* 148:42–57.
- 920 Olofsson, P., G. M. Foody, S. V. Stehman, and C. E. Woodcock. 2013. Making better use of accuracy
921 data in land change studies: Estimating accuracy and area and quantifying uncertainty using
922 stratified estimation. *Remote Sensing of Environment* 129:122–131.
- 923 Openshaw, S., and P. J. Taylor. 1979. A million or so correlation coefficients: Three experiments on
924 the modifiable areal unit problem. *Statistical applications in the spatial sciences* 21:127–144.
- 925 Pan, S. J., and Q. Yang. 2010. A Survey on Transfer Learning. *IEEE Transactions on Knowledge and*
926 *Data Engineering* 22:1345–1359.
- 927 Persello, C., V. A. Tolpekin, J. R. Bergado, and R. A. de By. 2019. Delineation of agricultural fields in
928 smallholder farms from satellite images using fully convolutional networks and combinatorial
929 grouping. *Remote Sensing of Environment* 231:111253.
- 930 PlanetTeam. 2018. Planet application program interface: In space for life on Earth.
931 <https://api.planet.com>, San Francisco, CA.
- 932 Pontius, R. G., and K. Si. 2014. The total operating characteristic to measure diagnostic ability for
933 multiple thresholds. *International Journal of Geographical Information Science* 28:570–583.

- 934 Qiu, S., Z. Zhu, and C. E. Woodcock. 2020. Cirrus clouds that adversely affect Landsat 8 images:
935 What are they and how to detect them? *Remote Sensing of Environment* 246:111884.
- 936 Rodriguez-Galiano, V. F., B. Ghimire, J. Rogan, M. Chica-Olmo, and J. P. Rigol-Sanchez. 2012. An
937 assessment of the effectiveness of a random forest classifier for land-cover classification. *ISPRS*
938 *Journal of Photogrammetry and Remote Sensing* 67:93–104.
- 939 Rulli, M. C., and P. D’Odorico. 2014. Food appropriation through large scale land acquisitions.
940 *Environmental Research Letters* 9:064030.
- 941 Samberg, L. H., J. S. Gerber, N. Ramankutty, M. Herrero, and P. C. West. 2016. Subnational
942 distribution of average farm size and smallholder contributions to global food production.
943 *Environmental Research Letters* 11:124010.
- 944 Searchinger, T. D., L. Estes, P. K. Thornton, T. Beringer, A. Notenbaert, D. Rubenstein, R. Heimlich,
945 R. Licker, and M. Herrero. 2015. High carbon and biodiversity costs from converting Africa’s wet
946 savannahs to cropland. *Nature Climate Change* 5:481–486.
- 947 Searchinger, T., R. Waite, C. Hanson, J. Ranganathan, P. Dumas, E. Matthews, and C. Klirs. 2019.
948 Creating a sustainable food future: A menu of solutions to feed nearly 10 billion people by 2050.
949 Final report. WRI.
- 950 Stehman, S. V., and G. M. Foody. 2019. Key issues in rigorous accuracy assessment of land cover
951 products. *Remote Sensing of Environment* 231:111199.
- 952 Sulla-Menashe, D., J. M. Gray, S. P. Abercrombie, and M. A. Friedl. 2019. Hierarchical mapping of
953 annual global land cover 2001 to present: The MODIS Collection 6 Land Cover product. *Remote*
954 *Sensing of Environment* 222:183–194.
- 955 Tong, X., M. Brandt, P. Hiernaux, S. Herrmann, L. V. Rasmussen, K. Rasmussen, F. Tian, T.
956 Tagesson, W. Zhang, and R. Fensholt. 2020. The forgotten land use class: Mapping of fallow fields
957 across the Sahel using Sentinel-2. *Remote Sensing of Environment* 239:111598.
- 958 Tuia, D., M. Volpi, L. Copa, M. Kanevski, and J. Munoz-Mari. 2011. A Survey of Active Learning
959 Algorithms for Supervised Remote Sensing Image Classification. *IEEE Journal of Selected Topics in*
960 *Signal Processing* 5:606–617.
- 961 Van Vliet, N., O. Mertz, T. Birch-Thomsen, and B. Schmook. 2013. Is There a Continuing Rationale
962 for Swidden Cultivation in the 21st Century? *Human Ecology* 41:1–5.
- 963 Visvalingam, M., and J. D. Whyatt. 1993. Line generalisation by repeated elimination of points. *The*
964 *Cartographic Journal* 30:46–51.
- 965 Von Braun, J. 2004. Small-scale farmers in a liberalized trade environment. Page 21.
- 966 Waldner, F., and F. I. Diakogiannis. 2020. Deep learning on edge: Extracting field boundaries from
967 satellite images with a convolutional neural network. *Remote Sensing of Environment* 245:111741.
- 968 Waldner, F., A. Schucknecht, M. Lesiv, J. Gallego, L. See, A. Pérez-Hoyos, R. d’Andrimont, T. de
969 Maet, J. C. L. Bayas, S. Fritz, O. Leo, H. Kerdiles, M. Díez, K. Van Tricht, S. Gilliams, A.

- 970 Shelestov, M. Lavreniuk, M. Simões, R. Ferraz, B. Bellón, A. Bégué, G. Hazeu, V. Stonacek, J.
971 Kolomaznik, J. Misurec, S. R. Verón, D. de Abelleira, D. Plotnikov, L. Mingyong, M. Singha, P.
972 Patil, M. Zhang, and P. Defourny. 2019. Conflation of expert and crowd reference data to validate
973 global binary thematic maps. *Remote Sensing of Environment* 221:235–246.
- 974 Wilson, A. M., and W. Jetz. 2016. Remotely Sensed High-Resolution Global Cloud Dynamics for
975 Predicting Ecosystem and Biodiversity Distributions. *PLOS Biology* 14:e1002415.
- 976 Wulder, M. A., J. C. White, T. R. Loveland, C. E. Woodcock, A. S. Belward, W. B. Cohen, E. A.
977 Fosnight, J. Shaw, J. G. Masek, and D. P. Roy. 2016. The global Landsat archive: Status,
978 consolidation, and direction. *Remote Sensing of Environment* 185:271–283.
- 979 Xiong, J., P. S. Thenkabail, J. C. Tilton, M. K. Gumma, P. Teluguntla, A. Oliphant, R. G. Congalton,
980 K. Yadav, and N. Gorelick. 2017. Nominal 30-m Cropland Extent Map of Continental Africa by
981 Integrating Pixel-Based and Object-Based Algorithms Using Sentinel-2 and Landsat-8 Data on
982 Google Earth Engine. *Remote Sensing* 9:1065.
- 983 Ye, S., R. G. Pontius, and R. Rakshit. 2018. A review of accuracy assessment for object-based image
984 analysis: From per-pixel to per-polygon approaches. *ISPRS Journal of Photogrammetry and*
985 *Remote Sensing* 141:137–147.
- 986 Yizong Cheng. 1995. Mean shift, mode seeking, and clustering. *IEEE Transactions on Pattern Analysis*
987 *and Machine Intelligence* 17:790–799.
- 988 Zeng, Z., L. Estes, A. D. Ziegler, A. Chen, T. Searchinger, F. Hua, K. Guan, A. Jintrawet, and E. F.
989 Wood. 2018. Highland cropland expansion and forest loss in Southeast Asia in the twenty-first
990 century. *Nature Geoscience* 11:556–562.
- 991 Zhang, Y., B. Guindon, and J. Cihlar. 2002. An image transform to characterize and compensate for
992 spatial variations in thin cloud contamination of Landsat images. *Remote Sensing of Environment*
993 82:173–187.
- 994 Zhu, X. X., D. Tuia, L. Mou, G.-S. Xia, L. Zhang, F. Xu, and F. Fraundorfer. 2017. Deep learning in
995 remote sensing: A review. *IEEE Geoscience and Remote Sensing Magazine* 5:8–36.
- 996 Zhu, Z., and C. E. Woodcock. 2012. Object-based cloud and cloud shadow detection in Landsat
997 imagery. *Remote Sensing of Environment* 118:83–94.